Digital Three-Dimensional Imaging Techniques Provide New Analytical Pathways for Malacological Research

Authors: Ziegler, Alexander, Bock, Christian, Ketten, Darlene R., Mair, Ross W., Mueller, Susanne, et al.

Source: American Malacological Bulletin, 36(2) : 248-273

Published By: American Malacological Society

URL: https://doi.org/10.4003/006.036.0205

Amer. Malac. Bull. **36**(2): 248–273 (2018)

Digital three-dimensional imaging techniques provide new analytical pathways for malacological research

Alexander Ziegler[1], Christian Bock[2], Darlene R. Ketten[3], Ross W. Mair[4], Susanne Mueller[5], Nina Nagelmann[6], Eberhard D. Pracht[7], and Leif Schröder[8]

[1]Institut für Evolutionsbiologie und Ökologie, Rheinische Friedrich-Wilhelms-Universität, An der Immenburg 1, 53121 Bonn, Germany. aziegler@evolution.uni-bonn.de

[2]Integrative Ökophysiologie, Alfred-Wegener-Institut Helmholtz-Zentrum für Polar- und Meeresforschung, Am Handelshafen 12, 27570 Bremerhaven, Germany.

[3]Marine Research Facility, Woods Hole Oceanographic Institution, 266 Woods Hole Road, Woods Hole, Massachusetts 02543, U.S.A.

[4]Center for Brain Science, Harvard University, 52 Oxford Street, Cambridge, Massachusetts 02138, U.S.A.

[5]Department of Experimental Neurology and Center for Stroke Research Berlin, Charité-Universitätsmedizin Berlin, corporate member of Freie Universität Berlin, Humboldt-Universität zu Berlin, and Berlin Institute of Health, Charitéplatz 1, 10117 Berlin, Germany.

[6]Institut für Klinische Radiologie, Universitätsklinikum Münster, Albert-Schweitzer-Campus 1, 48149 Münster, Germany.

[7]MR-Physik, Deutsches Zentrum für Neurodegenerative Erkrankungen, Sigmund-Freud-Straße 27, 53127 Bonn, Germany.

[8]Molekulare Bildgebung, Leibniz-Forschungsinstitut für Molekulare Pharmakologie, Robert-Rössle-Straße 10, 13125 Berlin, Germany.

Abstract: Research on molluscan specimens is increasingly being carried out using high-throughput molecular techniques. Due to their efficiency, these technologies have effectively resulted in a strong bias towards genotypic analyses. Therefore, the future large-scale correlation of such data with the phenotype will require a significant increase in the output of morphological studies. Three-dimensional (3D) scanning techniques such as magnetic resonance imaging (MRI) or computed tomography (CT) can achieve this goal as they permit rapidly obtaining digital data non-destructively or even entirely non-invasively from living, fixed, and fossil samples. With a large number of species and a relatively complex morphology, the Mollusca would profit from a more widespread application of digital 3D imaging techniques. In order to provide an overview of the capacity of various MRI and CT techniques to visualize internal and external structures of molluscs, more than twenty specimens ranging in size from a few millimeters to well over one meter were scanned *in vivo* as well as *ex vivo*. The results show that all major molluscan organ systems can be successfully visualized using both MRI and CT. The choice of a suitable imaging technique depends primarily on the specimen's life condition, its size, the required resolution, and possible invasiveness of the approach. Apart from visual examples derived from more than two dozen scans, the present article provides guidelines and best practices for digital 3D imaging of a broad range of molluscan taxa. Furthermore, a comprehensive overview of studies that previously have employed MRI or CT techniques in malacological research is given.

Key words: morphomics, digital morphology, phenomics, scanning, mollusc

Extant representatives of the Mollusca (Protostomia: Lophotrochozoa) have been extensively analyzed in the last decades using molecular techniques, lately in particular with high-throughput phylogenomic tools (Giribet 2008, Kocot *et al.* 2011, Smith *et al.* 2011, Smith *et al.* 2013, Dunn *et al.* 2014, Kocot *et al.* 2017). Because of constantly increasing speed, reliability, and cost-efficiency of these technologies, ever more extensive genomic research is bound to be conducted in malacology. In comparison, the phenotype has received less attention in recent years (Sigwart and Lindberg 2015), a development that can be attributed to a general shift in scientific focus away from organismic and towards molecular research. In addition, this has also been the consequence of technical, methodological, and logistical impediments in structural research (Giribet 2010, Giribet 2015). Consequently, the amount of molecular and morphological data available for specific molluscan taxa may be hugely disparate, often showing a strong bias towards molecular analysis (Sigwart and Lindberg 2015). However, the increasingly widespread application of digital three-dimensional (3D) imaging techniques in zoology is reinvigorating interest in morphological analyses by providing researchers with tools that permit conducting studies at a significantly more rapid pace (Giribet 2015, Wanninger 2015). In particular, these imaging techniques generate large amounts of morphological data in a digital format that could be used in conjunction with digital data from molecular techniques to answer a variety of open questions in malacological research.

The two main approaches involving the application of techniques suitable for digital morphology (Ziegler *et al.* 2010) have – in analogy to molecular techniques – been coined phenomics and morphomics. The first concept aims to obtain large amounts of information on the varying structural effects of genetic mutations (Gerlai 2002, Houle 2010) in order to link genomic data to the growth, performance, and composition of an entire organism (Furbank and Tester 2011, Yang *et al.* 2013). This may involve the use of digital 3D imaging techniques, but can also be accomplished using less complex methodologies, *e.g.*, photography. In contrast, morphomics is directly centered on a large-scale application of invasive or non-invasive 3D digital imaging techniques that permit collecting organismic data comprehensively and at a rapid pace (Altenberg 2005, Lucocq *et al.* 2014, Chughtai *et al.* 2016). With an estimated 70,000 to 76,000 described recent species (Rosenberg 2014), the Mollusca constitute one of the largest metazoan taxa and are therefore a natural target for an accelerated, phenomic or morphomic approach as pointed out previously for cephalopods (Xavier *et al.* 2015). This concept applies particularly to Bivalvia and Gastropoda, which have the highest diversity within molluscs (Aguilera *et al.* 2017).

The Mollusca can be divided into the spicule-bearing Aculifera that include Chaetodermomorpha, Neomeniomorpha, and Polyplacophora and the shell-bearing Conchifera comprising Bivalvia, Scaphopoda, Gastropoda, Monoplacophora, and Cephalopoda (Wanninger and Wollesen 2018). External structures and internal hard parts provide reliable landmarks for taxonomic or phylogenetic inferences, but there are a limited number of informative characters. Internal soft tissues provide more characters, but may be affected by the invasiveness of the traditionally conducted dissections that do not permit a comprehensive analysis of organ systems in their natural context. The potential for damage from dissection has also dissuaded the systematic re-study of rare and valuable specimens, including type material. As digital imaging techniques have been demonstrated to be effective tools for the non-invasive visualization and reconstruction of the relative position of internal and external structures in molluscs (Sutton 2008, Hoffmann *et al.* 2014, Xavier *et al.* 2015), a more widespread use of these techniques would support elucidating molluscan morphology and anatomy on a larger scale.

A number of 3D imaging techniques can be employed to study animal morphology and anatomy non-destructively or even entirely non-invasively (Ziegler *et al.* 2008, Boistel *et al.* 2011, Ziegler 2012, Zanette *et al.* 2014, Gutiérrez *et al.* 2018). These technologies include magnetic resonance imaging (MRI), a technique based on the principle of nuclear magnetic resonance (NMR) as well as computed tomography (CT), which relies on differences in X-ray attenuation of biological tissues (Table 1). Both modalities have expanded and diversified considerably in the last two decades, resulting in the availability of more specialized applications such as functional MRI (fMRI), diffusion tensor imaging (DTI), micro-computed tomography (μCT), or synchrotron-based μCT (SRμCT). All of these scanning techniques generate digital data displayed initially as sectional images, but which are also suitable for multiple angle reformatting and for 3D visualization. Presumably of greatest importance, these techniques provide data adequate for online archiving and dissemination in specialized repositories analogous to those for molecular data.

To promote a more widespread application of digital morphology in malacological research, the principle aim of the present contribution is to provide a comprehensive overview of results derived from different CT- and MRI-based imaging modalities applied to representative molluscan taxa. In addition, the article sets out to ascertain if living, freshly fixed, and museum specimens are equally suitable for analyses using digital 3D imaging techniques and explores the potential of various commercial and free software packages to visualize molluscan morphology and anatomy with a high level of precision. Furthermore, protocols as well as best practices for scanning a diverse array of extant specimens ranging in length from millimeters to meters are provided. Finally, the present paper gives a broad overview of studies that have successfully employed digital 3D imaging techniques to analyze molluscan form and function.

MATERIALS AND METHODS

Specimens

A total of 21 specimens from 18 different genera were analyzed. The material was obtained from field trips, scientific cruises, museum collections, or beachcombing and covers a broad range of parameters including size (millimeters, centimeters, meters), life condition (*in vivo, ex vivo*), fixation (Bouin's solution, formalin, ethanol), preservation (wet, dry), as well as ontogenetic stage (embryo, juvenile, subadult, adult). Where applicable, specimens were relaxed by adding 3-7% $MgCl_2$ to sea water prior to fixation. In total, 26 scans were made using five different CT and MRI techniques.

Micro-computed tomography

Scans of smaller specimens were conducted using various X-ray tube μCT systems (Table 2): a Phoenix Nanotom with a detector size of 2,304 x 2,304 px (GE Sensing & Inspection Technologies, Wunstorf, Germany), an X-TEK HMX-ST 225 with a detector size of 2,000 x 2,000 px (Nikon Metrology, Leuven, Belgium), and a SkyScan 1272 with a detector size of 4,904 x 3,280 px (Bruker microCT, Kontich, Belgium). To prevent movement artifacts during scanning, specimens were either placed inside plastic tubes and mechanically fixed using thin plastic rods or were attached to a thin metal rod using orthodontic wax.

Table 1. Generalized properties of digital three-dimensional imaging techniques employed in the present study.

	Micro-computed tomography	**Contrast-enhanced micro-computed tomography**	**Computed tomography**	**Preclinical magnetic resonance imaging**	**Clinical magnetic resonance imaging**
Field of view	50 µm-500 mm	50 µm-500 mm	50-500 mm	10-150 mm	100-300 mm
Voxel resolution	50 nm-100 µm	50 nm-100 µm	100 µm-2 mm	35-150 µm	100 µm-3 mm
2D single slice imaging	Impossible, only 2D X-ray projection images	Impossible, only 2D X-ray projection images	Possible in non-helical mode	Possible	Possible
3D region-of-interest scanning	Possible	Possible	Possible	Possible	Possible
Acquisition time for 3D scans	Minutes to hours, single 2D X-ray projection within seconds	Minutes to hours, single 2D X-ray projection within seconds	Minutes to hours, single 2D X-ray projection within seconds	Minutes to hours, single 2D section within seconds	Minutes to hours, single 2D section within seconds
Dataset size	MB-PB	MB-PB	MB-PB	MB-GB	MB-GB
Life condition	Usually *ex vivo* due to increased X-ray dose	*Ex vivo*	*In vivo* and *ex vivo*	*In vivo* and *ex vivo*	*In vivo* and *ex vivo*
Scanning medium	Air, several liquids possible	Ethanol, water, air	Air, liquids (incl. frozen)	Distilled water, several other liquids possible	Air, several liquids possible
Hard part visualization	Excellent	Excellent	Excellent	Limited, negative contrast due to surrounding tissues	Limited, negative contrast due to surrounding tissues
Soft part visualization	Limited	Excellent due to contrast agent	Limited	Excellent	Excellent
Potential artifacts	Beam hardening, ringing, partial volume, photon starvation, undersampling, movement, pixel blooming	Beam hardening, ringing, partial volume, photon starvation, undersampling, movement, pixel blooming	Beam hardening, ringing, partial volume, photon starvation, undersampling, movement, pixel blooming	Movement, Gibbs ringing, chemical shift, aliasing, susceptibility caused by air or magnetic particles	Movement, Gibbs ringing, chemical shift, aliasing, susceptibility caused by air or magnetic particles

Table 2. List of specimens analyzed using computed tomography techniques. AVG = averages, CUR = source current, EXP = exposure time, FIL = filter, FOV = field of view, MCZ = Museum of Comparative Zoology (Cambridge, Massachusetts, U.S.A.), MTX = matrix size, RES = voxel resolution, STE = step size, TA = acquisition time, TL = total length, VOL = source voltage, ZMB = Museum für Naturkunde (Berlin, Germany), ZMK = Zoologisk Museum København (Copenhagen, Denmark).

Scan	Taxon	Specimen	Scanning parameters	Figure
1	*Lepidochitona cinerea* (Linnaeus, 1767)	Unvouchered, *ex vivo*, adult, 15.5 mm TL, Sylt (North Sea)	Phoenix Nanotom, 100 kV VOL, 130 μA CUR, 0.2 mm Cu FIL, 1,000 ms EXP, 3 AVG, 0.4° STE, 8 x 8 x 8 μm RES, 1 h 2 min TA	1
2	*Leptochiton asellus* (Gmelin, 1791)	Unvouchered, *ex vivo*, adult, 13 mm TL, Heligoland (North Sea)	SkyScan 1272, 70 kV VOL, 142 μA CUR, 0.5 mm Al FIL, 834 ms EXP, 4 AVG, 0.4° STE, 8 x 8 x 8 μm RES, 34 min 31 s TA	2A-G
3	*Leptochiton asellus* (Gmelin, 1791)	Unvouchered, *ex vivo*, adult, 13 mm TL, Heligoland (North Sea)	SkyScan 1272, 60 kV VOL, 166 μA CUR, 0.25 mm Al FIL, 3,135 ms EXP, 3 AVG, 0.1° STE, 600 x 600 x 600 nm RES, 5 h 56 min 57 s TA	2H-J
4	*Cerastoderma edule* (Linnaeus, 1758)	Unvouchered, *ex vivo*, adult, 21 mm TL, Sylt (North Sea)	Phoenix Nanotom, 100 kV VOL, 160 μA CUR, 0.2 mm Cu FIL, 750 ms EXP, 2 AVG, 0.4° STE, 13 x 13 x 13 μm RES, 1 h 16 min TA	3A-D
5	*Cerithium litteratum* (Born, 1778)	Unvouchered, *ex vivo*, adult, 22.5 mm TL, Naples (Gulf of Mexico)	Phoenix Nanotom, 100 kV VOL, 160 μA CUR, 0.2 mm Cu FIL, 1,000 ms EXP, 4 AVG, 0.4° STE, 25 x 25 x 25 μm RES, 1 h 47 min TA	3E-H
6	*Nautilus pompilius* Linnaeus, 1758	MCZ 380017, *ex vivo*, adult, 77 mm TL, Gilbert Islands (Pacific Ocean)	HMX ST 225, 80 kV VOL, 120 μA CUR, 0.1 mm Cu FIL, 1 AVG, 0.4° STE, 42.33 x 42.33 x 42.33 μm RES, 48 min TA	3I-L
7	*Dosidicus gigas* (d'Orbigny [in 1834-1847], 1835)	D-gig01/S-353773-US, *ex vivo*, adult, 1.55 m TL, California (Pacific Ocean)	Somatom Volume Zoom, 120 kV VOL, 134 mAs CUR, 750 ms EXP, 0.4° STE, 350 x 350 mm FOV, 683 x 683 x 1,000 mm RES, 6 min 30 s TA (x4, batch scan)	4
8	*Acanthochitona crinita* (Pennant, 1777)	Unvouchered, *ex vivo*, adult, 32 mm TL, Concarneau (Atlantic Ocean)	SkyScan 1272, 100 kV VOL, 100 μA CUR, 0.11 mm Cu FIL, 1,050 ms EXP, 8 AVG, 0.4° STE, 1,632 x 1,092 px MTX, 12 x 12 x 12 μm RES, 1 h 16 min 43 s TA (x4, batch scan)	5A-C
9	*Spirula spirula* (Linnaeus, 1758)	ZMK 405, *ex vivo*, adult, 63 mm TL, Zavala (Indian Ocean)	SkyScan 1272, 100 kV VOL, 100 μA CUR, 0.11 mm Cu FIL, 2,600 ms EXP, 10 AVG, 0.3° STE, 2,452 x 1,640 px MTX, 10 x 10 x 10 μm RES, 5 h 29 min 18 s TA (x5, batch scan)	5D-G
10	*Muusoctopus* Gleadall, 2004	ZMB 240165, *ex vivo*, embryo, 12 mm TL, Bering Sea (Pacific Ocean)	SkyScan 1272, 80 kV VOL, 125 μA CUR, 1 mm Al FIL, 1,030 ms EXP, 10 AVG, 0.2° STE, 2,452 x 1,640 px MTX, 5 x 5 x 5 μm RES, 3 h 44 min 24 s TA	6

Computed tomography

Scans of larger specimens were made using a Somatom Volume Zoom helical CT system (SIEMENS Healthineers, Erlangen, Germany). Tube voltages employed were 120-140 kV and the radiographs were processed with an image matrix size of 512 x 512 px. The scans were performed as a series of four continual spirals, each of which was done with a table speed of 1 mm/s and 1 mm data block acquisition per tube rotation (Table 2). Partial soft part visualization was accomplished through selection of an ultrahigh kernel (U/H90) and extended scales with bone and soft tissue windowing using protocols frequently used for head and neck imaging in human diagnostics.

Contrast-enhanced micro-computed tomography

Formalin-fixed, ethanol-preserved specimens of one polyplacophoran and two cephalopod species were placed in 50 ml plastic tubes and stained using an 0.3% phosphotungstic acid (PTA) solution in 70% ethanol. Specimens were stained for four weeks each and placed inside plastic tubes filled with clean 70% ethanol directly prior to scanning (Table 2). The scans were made using a SkyScan 1272 μCT system with a detector size of 4,904 x 3,280 px (Bruker microCT).

Preclinical magnetic resonance imaging

Scans of smaller specimens were obtained using five different high-field preclinical MRI systems (Table 3): a

Table 3. List of specimens analyzed using magnetic resonance imaging techniques. AVG = averages, DTI = diffusion tensor imaging, FA = flip angle, FLASH = fast low angle shot, FMNH = Field Museum of Natural History (Chicago, Illinois, U.S.A.), FOV = field of view, MCZ = Museum of Comparative Zoology (Cambridge, Massachusetts, U.S.A.), MP-SAGE = magnetization-prepared spiral acquisition gradient echo, MSME = multi slice multi echo, MTX = matrix size, RARE = rapid acquisition relaxation enhancement, RES = voxel resolution, SE = spin echo, SEQ = sequence, TA = acquisition time, TE = echo time, TL = total length, TR = repetition time, ZMB = Museum für Naturkunde (Berlin, Germany).

Scan	Taxon	Specimen	Scanning parameters	Figure
11	*Cerastoderma edule* (Linnaeus, 1758)	Unvouchered, *ex vivo*, adult, 21 mm TL, Sylt (North Sea)	7 T PharmaScan 70/16, 3D FLASH SEQ, 30 ms TR, 6.66 ms TE, 35° FA, 31.2 x 31.2 x 31.2 mm FOV, 384 x 384 x 384 MTX, 12 AVG, 81 x 81 x 81 µm RES, 14 h 44 min 44 s TA	7A-C
12	*Mytilus edulis* Linnaeus, 1758	Unvouchered, *in vivo*, adult, 71 mm TL, Sylt (North Sea)	4.7 T BioSpec 47/40 DBX, 2D RARE SEQ, 12.367 ms TR, 183.6 ms TE, 180° FA, 100.5 x 100.5 mm FOV, 256 x 256 px MTX, 1 AVG, 393 x 393 x 2,000 µm RES, 1 min 14 s TA	7D-F
13	*Dendronotus frondosus* (Ascanius, 1774)	Unvouchered, *ex vivo*, adult, 24.5 mm TL, Concarneau (Atlantic Ocean)	7 T PharmaScan 70/16, 2D FLASH SEQ, 30 ms TR, 6.66 ms TE, 35° FA, 31.25 x 31.25 mm FOV, 384 x 384 MTX, 1 AVG, 81 x 81 x 313 µm RES, 24 min 11 s 52 ms TA	7G, H
14	*Carronella pellucida* (Alder & Hancock, 1843)	Unvouchered, *ex vivo*, adult, 25 mm TL, Castle Point (Atlantic Ocean)	7 T PharmaScan 70/16, 2D RARE SEQ, 3,500 ms TR, 36 ms TE, 42 x 42 mm FOV, 256 x 256 px MTX, 8 AVG, 164 x 164 x 500 µm RES, 11 min 12 s TA	7I
15	*Brachidontes exustus* (Linnaeus, 1758)	FMNH 243, *ex vivo*, juvenile, 16 mm TL, Vero Beach (Atlantic Ocean)	9.4 T BioSpec 94/20, 3D FLASH SEQ, 30 ms TR, 5.11 ms TE, 15° FA, 17.5 x 8.0 x 11.7 mm FOV, 440 x 200 x 296 px MTX, 4 AVG, 40 x 40 x 40 µm RES, 1 h 58 min 24 s TA	8A-C
16	*Ostrea edulis* Linnaeus, 1758	Unvouchered, *in vivo*, adult, 143 mm TL, Vigo (Atlantic Ocean)	9.4 T BioSpec 94/30, 2D RARE SEQ, 2,000 ms TR, 53.19 ms TE, 90° FA, 120 x 120 mm FOV, 512 x 512 px MTX, 8 AVG, 234 x 234 x 1,000 µm RES, 17 min 4 s TA	8D, E
17	*Crassostrea virginica* Gmelin, 1791	Unvouchered, *in vivo*, adult, 135 mm TL, Stump Sound (Atlantic Ocean)	4.7 T BioSpec 47/40 DBX, 2D RARE SEQ, 6,000 ms TR, 20.9 ms TE, 90° FA, 80 x 80 mm FOV, 128 x 128 px MTX, 8 AVG, 625 x 625 x 2,740 µm RES, 12 min 48 s TA	8F
18	*Pecten maximus* (Linnaeus, 1758)	Unvouchered, *in vivo*, adult, 99 mm TL, Vigo (Atlantic Ocean)	9.4 T BioSpec 94/30, 2D RARE SEQ, 3,000 ms TR, 45.51 ms TE, 90° FA, 120 x 120 mm FOV, 512 x 512 px MTX, 4 AVG, 234 x 234 x 1,000 µm RES, 12 min 46 s TA	8G
19	*Sepia officinalis* Linnaeus, 1758	Unvouchered, *ex vivo*, juvenile, 37 mm TL, Banyuls (Mediterranean Sea)	9.4 T BioSpec 94/20, 3D RARE SEQ, 600 ms TR, 35 ms TE, 180° FA, 36 x 15.2 x 15.2 mm FOV, 544 x 232 x 232 px MTX, 12 AVG, 66 x 66 x 66 µm RES, 13 h 27 min 22 s TA	8H, I
20	*Spirula spirula* (Linnaeus, 1758)	MCZ 93797, *ex vivo*, adult, 55 mm TL, St. Lucia (Caribbean Sea)	9.4 T BioSpec 94/20, 2D TurboRARE SEQ, 1,500 ms TR, 60.01 ms TE, 180° FA, 35 x 26 x 26 mm FOV, 584 x 432 x 256 px MTX, 8 AVG, 60 x 60 x 102 µm RES, 9 h 16 min 48 s TA	9A-C
21	*Sepia officinalis* Linnaeus, 1758	Unvouchered, *ex vivo*, sub-adult, 37 mm TL, Banyuls (Mediterranean Sea)	9.4 T AVANCE Ultrashield 400 WB Plus, 2D MSME SEQ, 7,446.6 ms TR, 40 ms TE, 180° FA, 35 x 17.5 mm FOV, 512 x 256 px MTX, 10 AVG, 30 x 30 x 100 µm RES, 8 h 28 min 21 s TA	9D
22	*Sepia officinalis* Linnaeus, 1758	Unvouchered, *ex vivo*, sub-adult, 37 mm TL, Banyuls (Mediterranean Sea)	9.4 T AVANCE Ultrashield 400 WB Plus, DTI SEQ, 12.5 s TR, 37.96 ms TE, 15 x 15 mm FOV, 256 x 256 px MTX, 1 AVG, 58.6 x 58.6 x 235 µm RES, 24 h 18 min 21 s TA	9E-G

Table 3. (Continued)

Scan	Taxon	Specimen	Scanning parameters	Figure
23	*Sepia omani* Adam & Rees, 1966	MCZ 380019, *ex vivo*, adult, 247 mm TL, Jiagarh (Indian Ocean)	3 T MAGNETOM Tim Trio, 3D FLASH SEQ, 150 ms TR, 4.7 ms TE, 72° FA, 200 x 100 x 67 mm FOV, 576 x 288 x 192 px MTX, 4 AVG, 347 x 347 x 347 µm RES, 9 h 10 min 25 s TA	10A, B
24	*Sepia officinalis* Linnaeus, 1758	Unvouchered, *in vivo*, adult, 341 mm TL, Woods Hole (Atlantic Ocean)	3 T Achieva, 2D RARE SEQ, 595.6 ms TR, 100 ms TE, 90° FA, 240 x 240 mm FOV, 1,200 x 1,200 px MTX, 3 AVG, 200 x 200 x 1,000 µm RES, 20 min TA	10C
25	*Sepia officinalis* Linnaeus, 1758	Unvouchered, *in vivo*, adult, 341 mm TL, Woods Hole (Atlantic Ocean)	3 T Achieva, 3D RARE SEQ, 1,700 ms TR, 190 ms TE, 90° FA, 60 x 60 x 60 mm FOV, 512 x 512 x 512 px MTX, 6 AVG, 117 x 117 x 117 µm RES, 25 min TA	10D, E
26	*Grimpoteuthis* Robson, 1932	ZMB 240160, *ex vivo*, adult, 290 mm TL, Tenji Seamount (Pacific Ocean)	7 T MAGNETOM, 3D MP-SAGE SEQ, 3,000 ms TR, 3.4 ms TE, 7° FA, 150 x 111 x 150 mm FOV, 536 x 396 x 536 px MTX, 37 AVG, 280 x 280 x 280 µm RES, 16 h 59 min TA	10F, G

horizontal 4.7 T BioSpec 47/40 equipped with a 50 mm triple tuneable surface coil (Bruker BioSpin MRI, Ettlingen, Germany), a horizontal 7 T PharmaScan 70/16 using a linear transmit-receive birdcage resonator with an inner diameter of 38 mm (Bruker BioSpin MRI), a horizontal 9.4 T BioSpec 94/20 using either a 20 mm CryoProbe transmit-receive surface resonator or a microcoil quadrature volume resonator with an inner diameter of 35 mm (Bruker BioSpin MRI), a horizontal 9.4 T Biospec 94/30 using a volume coil with 200 mm inner diameter (Bruker BioSpin MRI), and a vertical 9.4 T AVANCE 400WB Plus NMR spectrometer equipped for ^{1}H imaging using a linear volume resonator with 15 mm inner diameter (Bruker BioSpin MRI). Prior to scanning, ethanol-preserved specimens were gradually immersed in distilled water for a few hours, while living specimens were kept fully-immersed inside plastic containers filled with oxygenated sea water. In selected cases, fixed specimens were embedded in 1% low-melting agarose contrasted with Magnevist (Bayer Vital, Leverkusen, Germany) at a final concentration of 2 mM.

Clinical magnetic resonance imaging

Scans of larger specimens were carried out using three different high-field clinical MRI systems (Table 3): a 3 T MAGNETOM Tim Trio equipped with a 32-channel head coil (SIEMENS Healthineers), a 3 T Achieva using an 8-channel SENSE head receiving coil (Philips Healthcare, Amsterdam, Netherlands), and a 7 T MAGNETOM in combination with a 32-channel head coil (SIEMENS Healthineers). The living cephalopod specimen analyzed in the course of this study was anaesthetized and kept inside a plastic container partially filled with oxygenated sea water. Care and subsequent imaging was conducted under the direction of a licensed veterinarian and according to procedures set forth by the Institutional Animal Care and Use Committee as well as the Universities Federation for Animal Welfare (Boyle 2010, Budelmann 2010).

Data visualization

Computer hardware used for two-dimensional (2D) sectioning and 3D visualization was based on 64-bit Windows 7 or 10 operating systems running on multi-core processors with 6-128 GB random access memory (RAM) and graphic cards with 1-24 GB video RAM. The free software packages employed in this study were Drishti (Limaye 2012), DSI Studio (http://dsi-studio.labsolver.org), Acrobat Reader (Adobe Systems, San Jose, California, USA), and Fiji (Schindelin *et al.* 2012). The commercial software packages used were Adobe 3D Reviewer (Adobe Systems), Amira 6.5 (Thermo Fisher Scientific, Waltham, Massachusetts, U.S.A.), ParaVision 4-6 (Bruker BioSpin MRI), and VGSTUDIO MAX 3.2 (Volume Graphics, Heidelberg, Germany).

Data deposition

A MorphoBank project (#3107) was created as repository for selected digital 2D and 3D data generated in the course of this study (Ziegler *et al.* 2018). The deposited information includes one DTI data folder, 23 tomographic datasets, and 80 media files amounting to a total size of 2 GB.

RESULTS

Molluscs in general are characterized by a complex internal anatomy, a relative dominance of soft parts, and the presence of extensive fluid-filled cavities. These anatomical and morphological features render molluscs in principle ideal candidates for MRI (Ziegler *et al.* 2011). In contrast, molluscan hard parts are best studied using CT techniques, because this approach provides superior results with regard to 3D analyses of mineralized tissues. CT and MRI can thus be seen as complementary imaging techniques, although both permit visualizing soft tissues as well as mineralized structures under certain conditions.

Micro-computed tomography

Scan 1

Gray chiton, *Lepidochitona cinerea* (Polyplacophora: Lepidochitonidae), adult, 15.5 mm total length (TL), formalin-fixed, ethanol-preserved, dataset acquired *ex vivo,* scanned in ethanol (Table 2). A digitally reconstructed radiography (DRR) rendering illustrates that the chosen scan settings permit recognition of hard parts only, despite the presence of soft tissues in this ethanol-preserved sample (Fig. 1A). Virtual sections and volume renderings at different positions and from various viewpoints show that mineralized tissues such as valves (Fig. 1B), spiculae (Fig. 1C), radula (Fig. 1D), tegmentum (Fig. 1E), and pustules (Fig. 1F), but also X-ray-dense ingesta inside the posterior digestive tract (Fig. 1G) can be visualized using µCT. A close-up view of the radula (Fig. 1H) reveals that even individual radular teeth can be successfully differentiated at the given resolution. Because of its relatively large size, the dataset was binned (*i.e.,* down-sampled) from its original 8 µm to 16 µm isotropic voxel resolution (IVR) for online deposition. Due to the 3D nature of the tomographic data, this reduction in resolution by a factor of two results in a reduction of the dataset's volume by a factor of eight (*i.e.,* 2^3). While binning lowers resolution, it may result in an improved signal-to-noise ratio (SNR), thus artificially improving the visual aspect of the dataset.

Scan 2

Northern chiton, *Leptochiton asellus* (Polyplacophora: Leptochitonidae), adult, 13 mm TL, Bouin-fixed, ethanol-preserved, dataset acquired *ex vivo*, scanned in air (Table 2). For high-resolution scanning of an isolated chiton body part, the anterior valve was removed and air-dried. This scan was made to obtain an overview of the entire sample prior to scanning at higher resolutions (see below). A DRR rendering partly reveals the internal macrostructure of the anterior

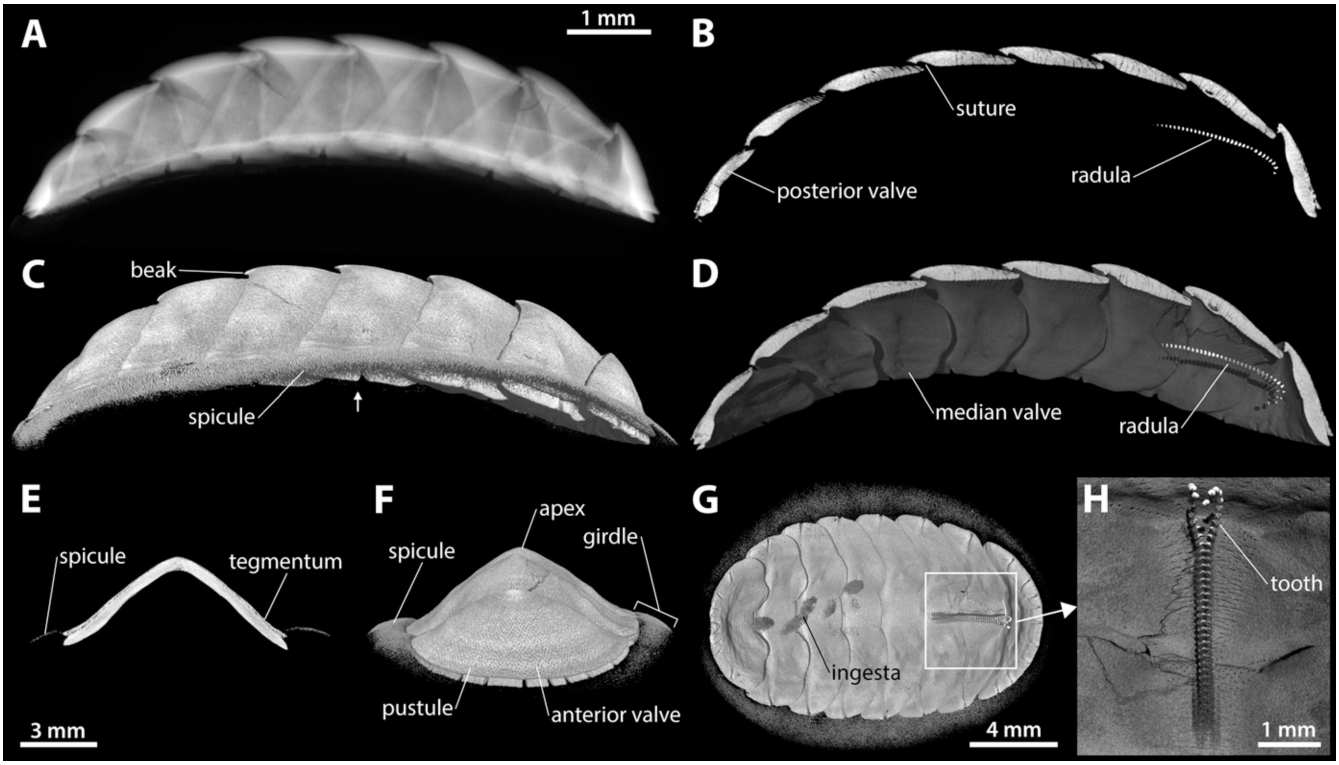

Figure 1. Micro-computed tomography data of an adult specimen of the polyplacophoran *Lepidochitona cinerea*. A. Digitally reconstructed radiograph rendering, lateral view with anterior to right. B. Virtual sagittal section at the level of the radula. C. Solid volume rendering. D. Virtual sagittal slicing of a solid volume rendering at the level of the radula. E. Virtual transverse section, position indicated by white arrow as in C. F. Solid volume rendering, anterior view. G. Solid volume rendering, ventral view with anterior to right. H. Close-up view of the radula. All renderings and virtual sections created using the commercial software Amira (A) and VGSTUDIO MAX (B-H) at 8 µm isotropic voxel resolution.

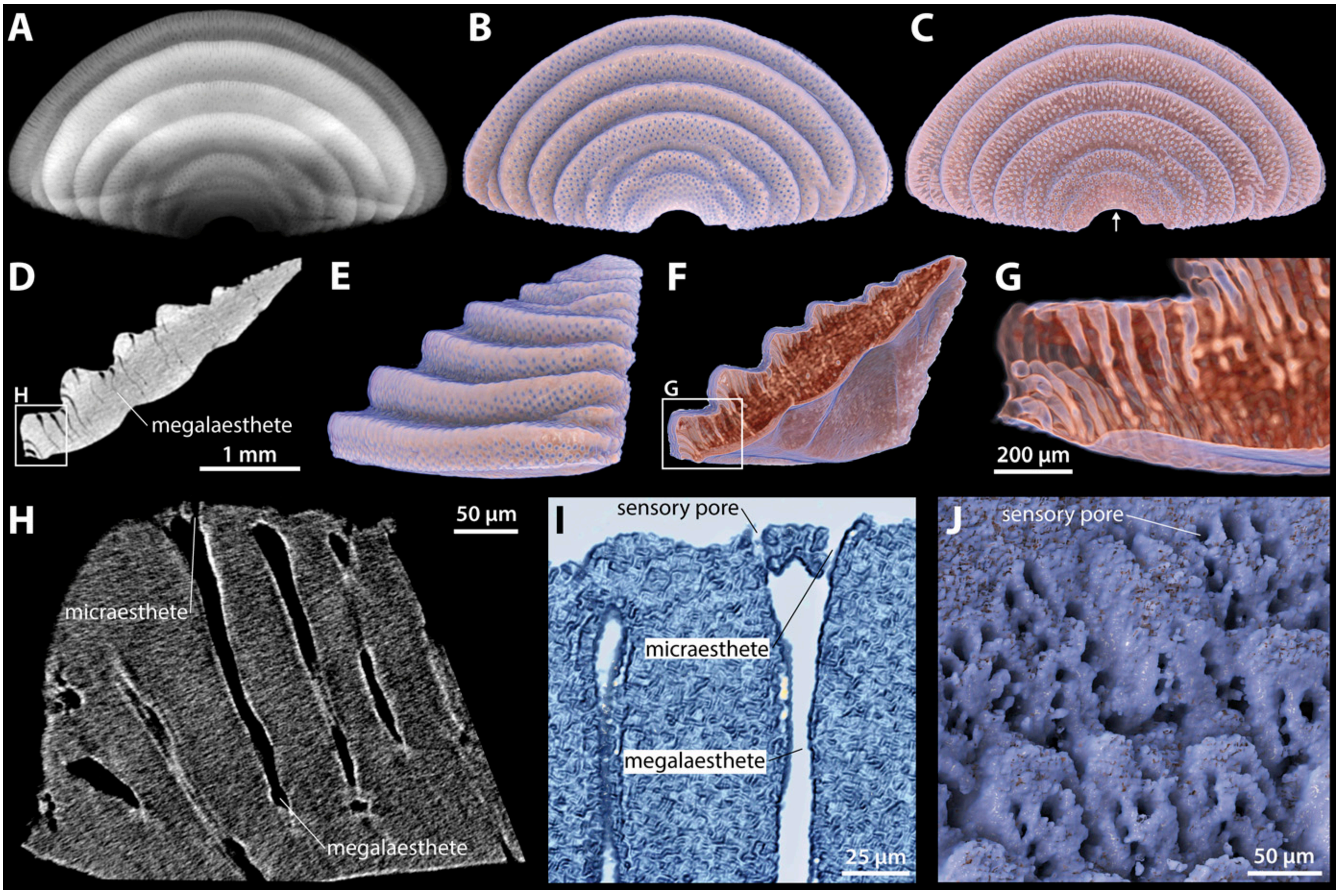

Figure 2. Micro-computed tomography data of the anterior valve of an adult specimen of the polyplacophoran *Leptochiton asellus*. The two datasets were acquired at 8 µm (A-G) and 600 nm (H-J) isotropic voxel resolution. A. Digitally reconstructed radiograph rendering, dorsal view with anterior facing up. B. Solid volume rendering. C. Semi-transparent volume rendering. D. Virtual sagittal section, anterior to left, position indicated by white arrow as in C. E. Solid volume rendering, lateral view. F. Virtual sagittal slicing of a solid volume rendering. G. Close-up as indicated in F. H. Close-up of the approximate area as indicated in D. I. Semi-transparent volume rendering of the distal area of a single megalaesthete**.** J. Dorsal view of part of the anterior valve. All renderings and virtual sections created using the commercial software Amira (A) as well as the free software Drishti (B, C, E-G, I, J) and Fiji (D, H).

valve (Fig. 2A), while a solid volume rendering can be used to show the superficial distribution of the sensory pores (Fig. 2B). However, a semi-transparent rendering (Fig. 2C) as well as a consecutive series of a virtual sagittal section (Fig. 2D), solid (Fig. 2E), and sliced (Fig. 2F, G) volume renderings are necessary to obtain a more comprehensive understanding of the underlying megalaesthete morphology. Despite the insight provided by this scan, a higher IVR is required to reveal smaller structures, specifically the micraesthetes.

Scan 3

Northern chiton, *Leptochiton asellus* (Polyplacophora: Leptochitonidae), adult, 13 mm TL, Bouin-fixed, ethanol-preserved, dataset acquired *ex vivo*, scanned in air (Table 2). In order to obtain a dataset with sub-micron resolution, only the anterior tip of the valve was scanned. As a virtual sagittal section through the resulting tomographic data shows, micraesthetes and megalaesthetes can now be differentiated (Fig. 2H). Close-up sagittal (Fig. 2I) and dorsal views (Fig. 2J) of the scanned region of interest (ROI) provide further insight into sensory pore morphology of this polyplacophoran species.

Scan 4

Common cockle, *Cerastoderma edule* (Bivalvia: Cardiidae), adult, 21 mm TL, Bouin-fixed, ethanol-preserved, dataset acquired *ex vivo*, scanned in ethanol (Table 2). As in the first scan (Fig. 1), the scanning parameters chosen here do not permit any differentiation of soft parts, despite their presence in this ethanol-preserved sample. This lack of soft tissue contrast is illustrated by a DRR rendering (Fig. 3A) as well

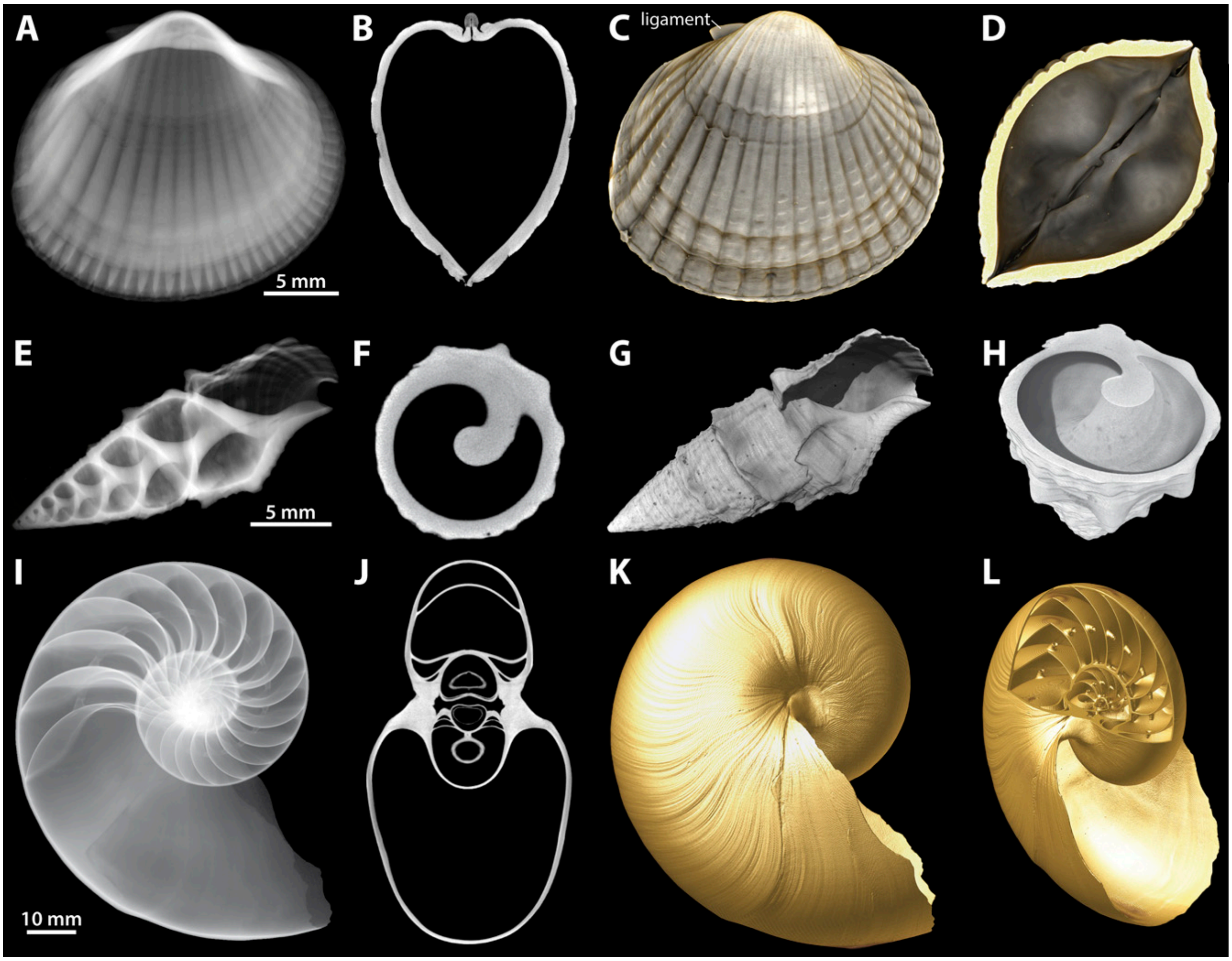

Figure 3. Micro-computed tomography data of adult specimens of the bivalve *Cerastoderma edule* (A-D), the gastropod *Cerithium litteratum* (E-H), and the cephalopod *Nautilus pompilius* (I-L). A, E, I. Digitally reconstructed radiograph rendering, lateral view. B, F, J. Virtual transverse section. C, G, K. Solid volume rendering. D, H, L. Virtual slicing of a solid volume rendering, oblique view. All renderings and virtual sections created using the commercial software Amira (A, E, I, K, L) and VGSTUDIO MAX (G, H) as well as the free software Fiji (B, F, J) and Drishti (C, D) at 26 µm (A-D), 25 µm (E-H), and 84.7 µm (I-L) isotropic voxel resolution.

as a virtual transverse section (Fig. 3B). However, despite its significantly lower density compared to the two valves, the ligament can still be identified (Fig. 3C). In addition, the previous as well as a further volume rendering permit obtaining an unobstructed view of all major hard parts, including the articulated hinge as seen from an internal viewpoint (Fig. 3D). These latter two images illustrate that visualization software can be used to generate false-colored renderings that closely approach the aspect of the specimen in real life (Fig. 3C).

Scan 5

Stocky cerith, *Cerithium litteratum* (Gastropoda: Cerithiidae), adult, 22.5 mm TL, dry shell, dataset acquired *ex vivo*, scanned in air (Table 2). A DRR rendering shows that the intricate internal coiling of the snail's shell can be easily visualized using µCT (Fig. 3E). However, a virtual horizontal section reveals that the shell's microstructure cannot be differentiated at the given resolution (Fig. 3F). Two volume renderings illustrate the capacity of modern visualization tools to provide a sense of depth through virtual shading (Fig. 3G) and slicing (Fig. 3H).

Scan 6

Chambered nautilus, *Nautilus pompilius* (Cephalopoda: Nautilidae), adult, 77 mm TL, dry shell, dataset acquired *ex vivo*, scanned in air (Table 2). A DRR rendering provides insight into the complex internal morphology of the chambered nautilus' shell (Fig. 3I). In addition, virtual sectioning can be used to generate views typically employed in nautilid taxonomy and systematics without the need to alter the specimen (Fig. 3J). False-colored volume renderings further illustrate that conventional (Fig. 3K) as well as entirely novel perspectives (Fig. 3L) of the nautilid shell can be obtained using digital μCT data.

Computed tomography

Scan 7

Humboldt squid, *Dosidicus gigas* (Cephalopoda: Ommastrephidae), adult, 1.55 m TL, frozen specimen, thawed prior to scanning, dataset acquired *ex vivo*, scanned in air (Table 2). A DRR rendering from a dorsal viewpoint illustrates the overall shape and scanning position of the animal (Fig. 4A). A virtual section at the level of the large, centrally located digestive gland reveals selected soft tissue organs such as gills or optic lobes, but also hard parts such as the statoliths (Fig. 4B). An impression of the external morphology can be obtained by solid volume rendering of the entire dataset (Fig. 4C), while selected internal organs can best be visualized using a semi-transparent rendering (Fig. 4D). Note the strongly X-ray absorbing content of the ink sac in contrast to the relatively weak attenuation of gladius as well as lower and upper beak (Fig. 4D).

Contrast-enhanced micro-computed tomography

Scan 8

Spiny chiton, *Acanthochitona crinita* (Polyplacophora: Acanthochitonidae), adult, 32 mm TL, Bouin-fixed, ethanol-preserved, dataset acquired *ex vivo*, scanned in ethanol (Table 2). Lateral and ventral views based on volume renderings of the 3D dataset show that all external hard and soft part features of this chiton such as valves, girdle, foot, or gills can be readily visualized at the given resolution (Fig. 5A, B). In addition, a virtual transverse section immediately posterior to the head demonstrates that major internal organ systems can be differentiated as well (Fig. 5C). In this particular image, individual lacunae located in the girdle and foot as well as the complex muscular disposition of the radula apparatus become apparent.

Scan 9

Ram's horn squid, *Spirula spirula* (Cephalopoda: Spirulidae), adult, 63 mm TL, formalin-fixed, ethanol-preserved, dataset acquired *ex vivo*, scanned in ethanol (Table 2). A DRR rendering from a lateral viewpoint suggests that the contrast agent has permeated the entire specimen, thus rendering all internal structures visible (Fig. 5D). Consequently, a virtual sagittal section reveals not only the hard part morphology of the animal with its coiled chambered shell, but also its soft part composition with buccal mass, statocysts, central nervous system, and various other internal organs (Fig. 5E). In

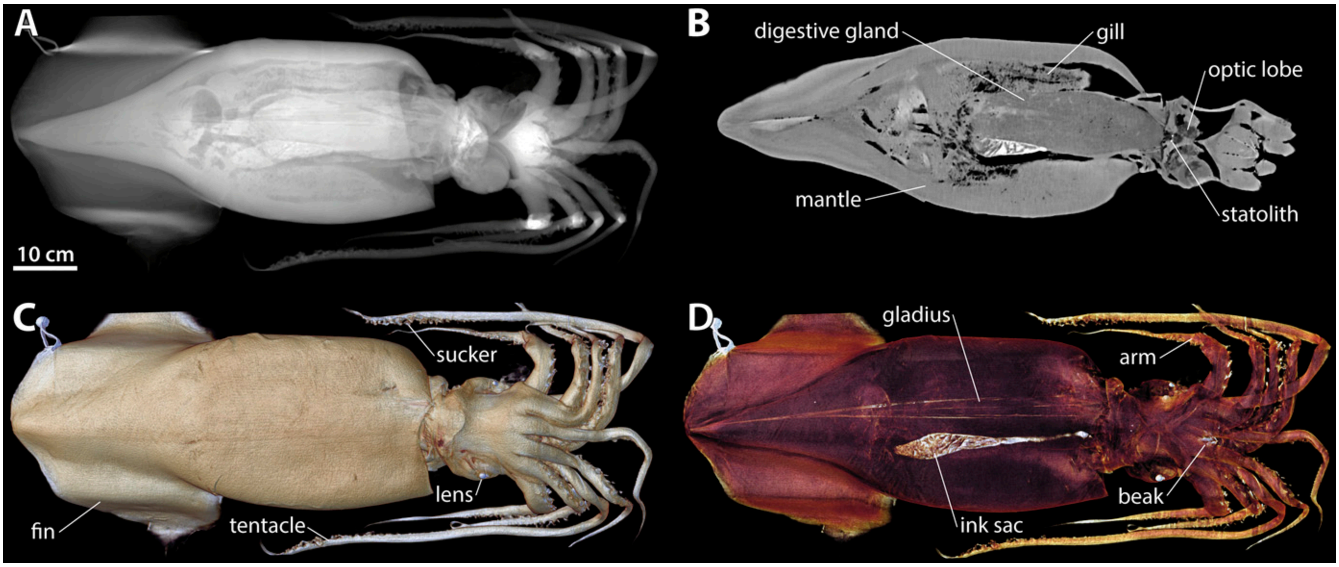

Figure 4. Computed tomography data of an adult specimen of the cephalopod *Dosidicus gigas*. A. Digitally reconstructed radiograph rendering, dorsal view with anterior facing right. B.Virtual horizontal section at the level of digestive gland and gills. C. Solid volume rendering showing external anatomical features. D. Semi-transparent volume rendering exposing selected internal organs. All renderings and virtual sections produced using the commercial software Amira at 683 μm isotropic voxel resolution.

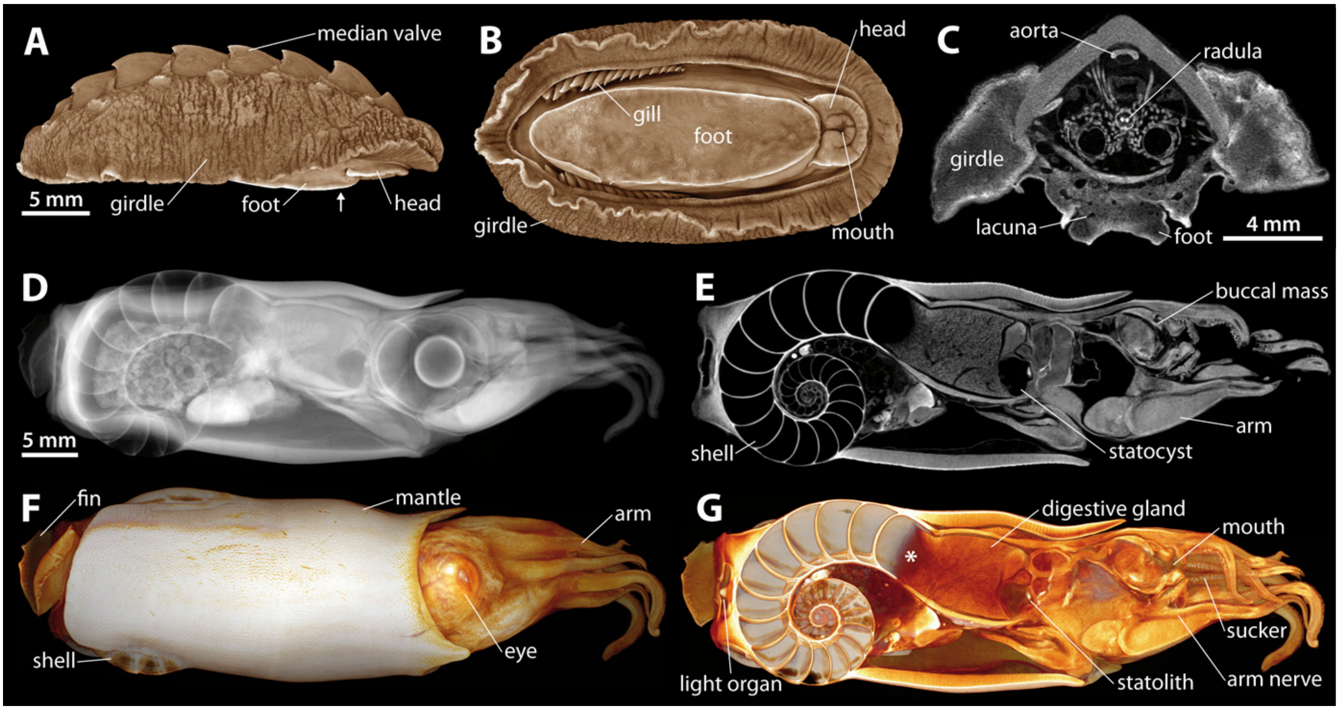

Figure 5. Micro-computed tomography data of contrast-enhanced adult specimens of the polyplacophoran *Acanthochitona crinita* (A-C) and the cephalopod *Spirula spirula* (D-G). A. Solid volume rendering, lateral view with anterior facing right. B. Solid volume rendering, ventral view. C. Virtual transverse section, position indicated by white arrow in (A). D. Digitally reconstructed radiograph rendering, lateral view with anterior to right. E. Virtual sagittal section at the level of the right statocyst. F. Solid volume rendering. G. Virtual slicing of a solid volume rendering at the level of the digestive gland. Asterisk indicates region with insufficient penetration of the contrast agent. All renderings and virtual sections created using the free software Drishti (A, B) and Fiji (C) as well as the commercial software Amira (D-G) at 24 µm (A-C) and 40 µm (D-G) isotropic voxel resolution.

addition, the 3D dataset can be used to visualize the external aspect of the animal with arms, tentacles, eyes, mantle, and fins (Fig. 5F). However, as a virtual slicing of a volume rendering seen from a lateral viewpoint shows, a small area at the posterior end of the digestive gland has not been stained (Fig. 5G). Despite several weeks of immersion in the contrast agent and occasional flushing of the mantle cavity, diffusion of PTA into this part of the sample was not achieved.

Scan 10

Inkless octopus, *Muusoctopus* sp. (Cephalopoda: Enteroctopodidae), embryo, 12 mm TL, formalin-fixed, ethanol-preserved, dataset acquired *ex vivo*, scanned in ethanol (Table 2). This specimen was part of an egg clutch collected during a scientific cruise in the Northern Pacific Ocean (Werner *et al.* 2016). The embryo was removed from its egg, because the contrast agent was incapable of penetrating the egg envelope. A DRR rendering shows that in addition to the external morphology, several internal structures of the specimen are visible, including the eyes and digestive gland (Fig. 6A). A virtual horizontal section reveals that major organ systems such as digestive tract, sensory organs, nervous system, or respiratory structures can be differentiated without difficulty (Fig. 6B). Virtual slicing of the volume-rendered dataset in combination with a 2D overlay permit obtaining a more plastic impression of the animal's internal structural composition (Fig. 6C). Furthermore, volume renderings of the dataset allow visualizing various external structural features such as the arms, suckers, or mantle (Fig. 6D). Due to the 3D nature of the dataset, virtual slicing can be used to create any desired arbitrary section, thus revealing additional internal organs such as the systemic heart, the statocysts, or individual components of the central nervous system (Fig. 6E). In addition, selected internal organs were manually segmented and surface-rendered, an approach that permits precise volumetric analyses and visualization of selected structures (Fig. 6F). Note the relatively high number of averages (Table 2), a parameter that was chosen to improve SNR in this scan of a contrasted animal scanned in ethanol compared with non-contrasted specimens scanned in air (*e.g.*, scan 2). Due to the X-ray attenuation of the liquid surrounding the specimen, multiple averages or longer exposure times need to be applied to obtain a better SNR.

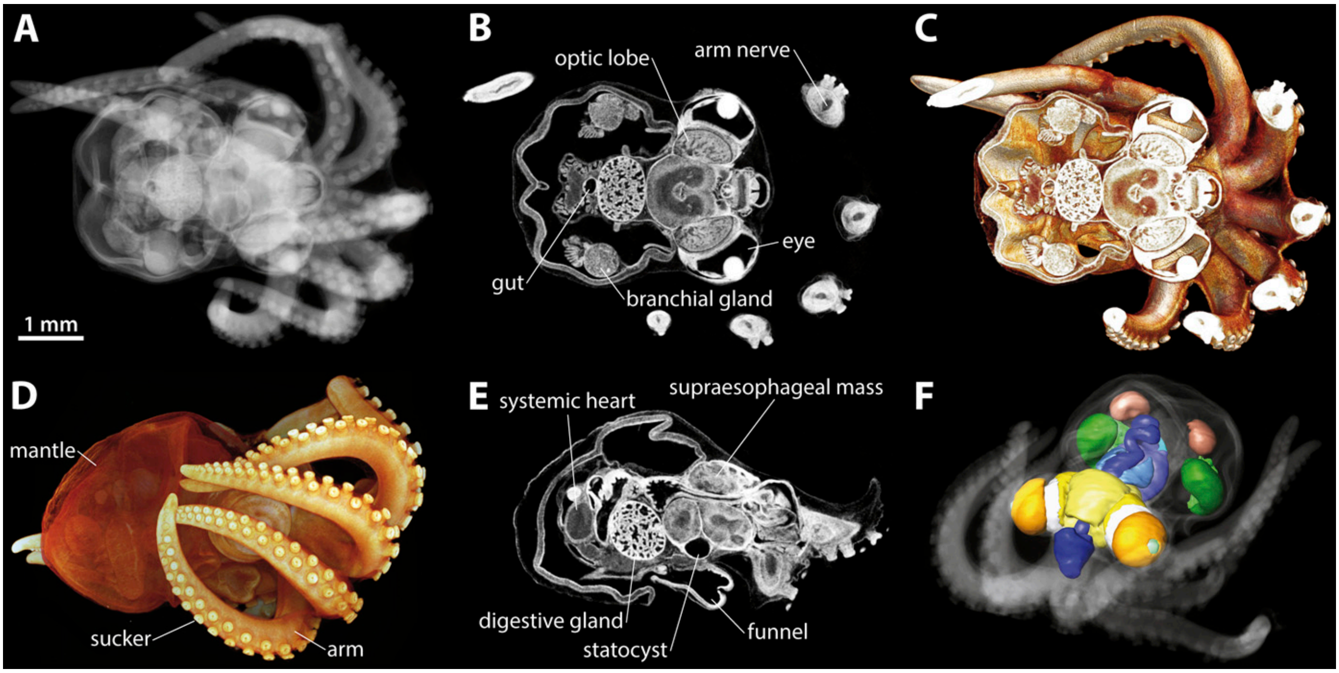

Figure 6. Micro-computed tomography data of a contrast-enhanced embryo of the cephalopod *Muusoctopus* sp. A. Digitally reconstructed radiograph rendering, dorsal view with anterior facing right. B. Virtual horizontal section at the level of the eyes. C. Virtual horizontal slicing of a solid volume rendering. D. Solid volume rendering, lateral view with anterior facing right. E. Virtual sagittal section at the level of the systemic heart. F. Digitally reconstructed radiograph rendering illustrating position of segmented internal organs, oblique anterodorsal view. Branchial gland = dark green, branchial heart = light brown, digestive tract = blue, eye = orange, gill = light green, nervous system = yellow, posterior salivary gland = light blue, white body = white. All renderings and virtual sections created using the commercial software Amira at 10 μm isotropic voxel resolution.

Preclinical magnetic resonance imaging

Scan 11

Common cockle, *Cerastoderma edule* (Bivalvia: Cardiidae), adult, 21 mm TL, formalin-fixed, ethanol-preserved, dataset acquired *ex vivo*, scanned in distilled water (Table 3). Virtual sections illustrate that a number of internal organs can be discerned using preclinical MRI, including the foot, adductor and retractor muscles, ligament, and various elements of the digestive tract (Fig. 7A, B). These structures can additionally be volume-rendered due to the relatively weak signal intensity of the surrounding water, a consequence of the specific MRI protocol chosen here (Fig. 7C). Note the susceptibility artifacts at the intersection of valves and the surrounding liquid – such distortions often occur at boundaries between tissues with different chemical properties (Fig. 7B).

Scan 12

Blue mussel, *Mytilus edulis* (Bivalvia: Mytilidae), adult, 71 mm TL, dataset acquired *in vivo*, scanned in seawater (Table 3). The imaging protocol employed here was a rapid 2D sequence with an acquisition time of slightly more than a minute. A series of orthogonal sections illustrates that even with such a reduced scanning time and relatively low resolution, all major internal organs of a common bivalve can be differentiated, in particular gills, adductor and retractor muscles (Fig. 7D) as well as mantle (Fig. 7E) and various components of the digestive tract (Fig. 7F).

Scan 13

Bushy-backed nudibranch, *Dendronotus frondosus* (Gastropoda: Dendronotidae), adult, 24.5 mm TL, formalin-fixed, ethanol-preserved, dataset acquired *ex vivo*, scanned in distilled water (Table 3). A virtual sagittal section through the dataset along the median plane shows that various internal and external structures can be differentiated, including the digestive tract, gonad, and foot (Fig. 7G). In order to test whether this scan could also be used for volumetric analyses, the original 2D dataset was zero-filled (*i.e.,* increased in resolution) from 313 μm to 81 μm along the Z axis, which resulted in a 3D dataset with 81 μm IVR. Visualization of this new image stack in the form of a virtually sliced volume rendering shows that the artificial increase in resolution along the third dimension can be used as a tool to acquire volumetric information from 2D MRI data (Fig. 7H). However, this artificial increase in resolution along the Z axis obviously cannot provide any additional structural information.

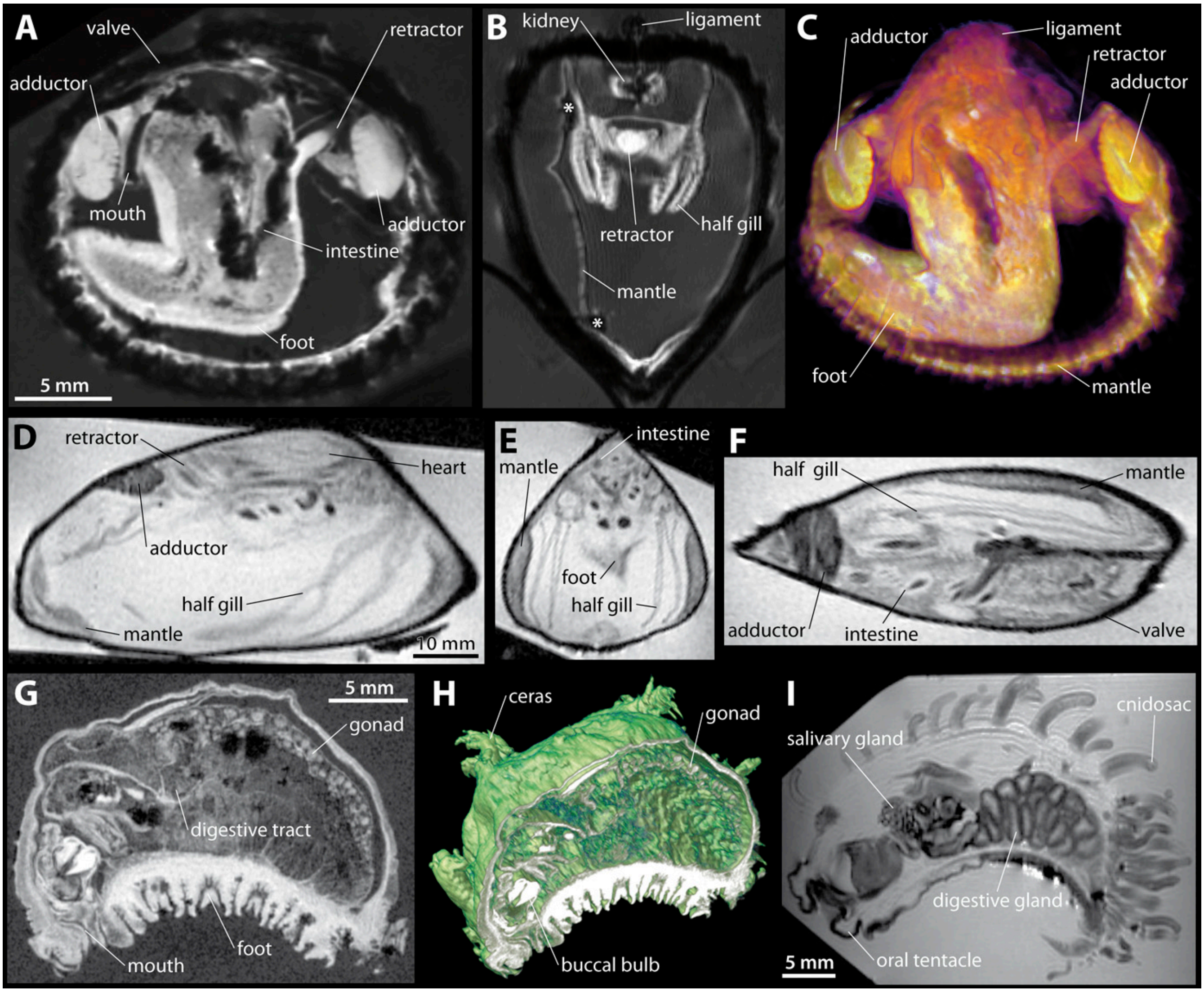

Figure 7. Magnetic resonance imaging data of adult specimens of the bivalves *Cerastoderma edule* (A-C) and *Mytilus edulis* (D-F) as well as the gastropods *Dendronotus frondosus* (G, H) and *Carronella pellucida* (I) obtained using high-field preclinical scanning systems. A. Virtual sagittal section at the level of the intestine, anterior facing left. B. Virtual transverse section at the level of the kidney. Asterisks denote susceptibility artifacts. C. Semi-transparent volume rendering, lateral view. D. Virtual sagittal section at the level of the stomach, anterior facing right. E. Virtual transverse section at the level of the foot. F. Virtual horizontal section at the level of the adductor, anterior facing right. G. Virtual sagittal section at the level of the mouth, anterior facing left. H. Virtual sagittal slicing of a solid volume rendering, oblique anterodorsal view. I. Virtual sagittal section at the level of the digestive gland, anterior to left. All renderings and virtual sections created using the free software Fiji (A-C), the proprietary scanner software ParaVision (D-F, I), and the commercial software Amira (G, H) at 40.5 µm isotropic (A-C), 39.3 x 39.3 x 2,000 µm (D-F), 40.5 µm isotropic (G, H), and 164 x 164 x 500 µm (I) voxel resolution.

Scan 14

Red-gilled nudibranch, *Carronella pellucida* (Gastropoda: Flabellinidae), adult, 25 mm TL, Bouin-fixed, ethanol-preserved, dataset acquired *ex vivo*, scanned in distilled water (Table 3). A single virtual sagittal section illustrates that in less than a quarter of an hour all major internal structures as well as external structures of a nudibranch can be visualized using preclinical MRI (Fig. 7I).

Scan 15

Scorched mussel, *Brachidontes exustus* (Bivalvia: Mytilidae), juvenile, 16 mm TL, ethanol-fixed, ethanol-preserved, dataset

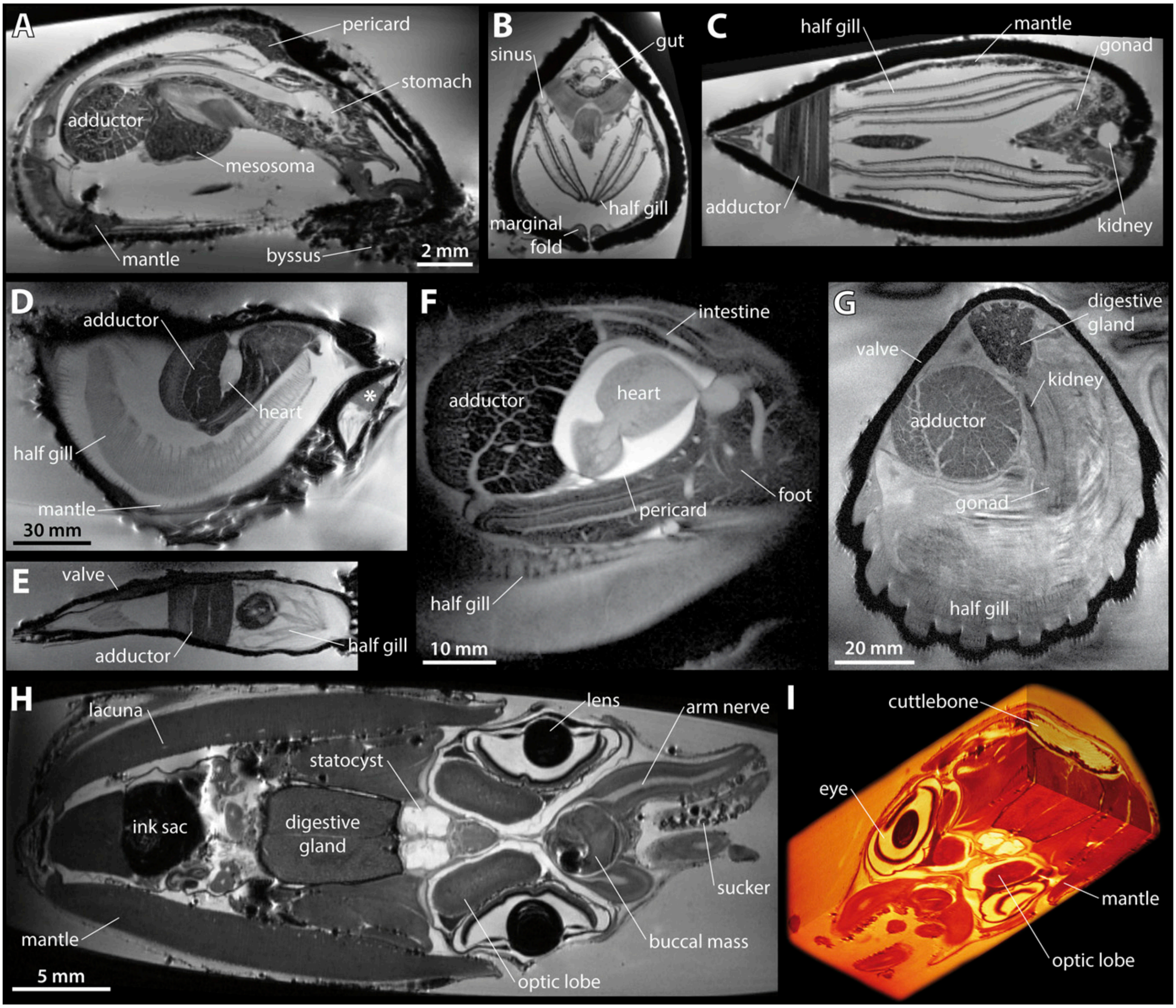

Figure 8. Magnetic resonance imaging data of adult specimens of the bivalves *Brachidontes exustus* (A-C), *Ostrea edulis* (D, E), *Crassostrea virginica* (F), and *Pecten maximus* (G) as well as the cephalopod *Sepia officinalis* (H, I) obtained using high-field preclinical scanning systems. A. Virtual sagittal section, anterior to right. B. Virtual transverse section. C. Virtual horizontal section, anterior to right. D. Virtual sagittal section at the level of the gills, anterior to right. Asterisk indicates a smaller specimen attached to the animal originally studied. E. Virtual horizontal section at the level of the adductor. F. Virtual sagittal section through a region of interest surrounding heart and adductor muscle, anterior to right. G. Virtual sagittal section, anterior facing right. H. Virtual horizontal section at the level of the statocysts, anterior to right. I. Composite figure showing sagittal, transverse, and horizontal false-colored virtual sections, oblique anterodorsal view. All renderings and virtual sections created using the free software Fiji (A-C), the proprietary software ParaVision (D-G), and the commercial software Amira (H, I) at 20 μm isotropic (A-C), 234 x 234 x 1,000 μm (D, E), 625 x 625 x 2,740 μm (F), 234 x 234 x 1,000 μm (G), and 33 μm isotropic (H, I) voxel resolution.

acquired *ex vivo*, scanned in agarose (Table 3). A virtual sagittal section shows that the chosen scanning parameters permit unambiguous identification of a considerable amount of internal structures such as the adductor muscles, mesosoma, stomach, and pericard (Fig. 8A). Further internal organs that can be observed are elements of the digestive tract, respiratory structures, and circulatory system (Fig. 8B), but also components of the excretory and reproductive systems (Fig. 8C). In this particular scan, a surface instead of a volume coil was used, which resulted in a notable shading gradient within the dataset. The source of this particular artifact is the surface coil itself, which has an optimal sensitivity at the center of the field of view (FOV) and therefore can cover only a certain part of the measured volume with homogenous signal intensity. However, such shading gradients can usually be removed from 2D as well as 3D tomographic image stacks by employing the *Polynomial Shading Corrector*, a plugin available for Fiji.

Scan 16

European flat oyster, *Ostrea edulis* (Bivalvia: Ostreidae), adult, 143 mm TL, dataset acquired *in vivo*, scanned in sea water (Table 3). Similar to the specimen of *M. edulis* (scan 12), virtual sections through this 2D dataset illustrate that despite the short acquisition times typically used for *in vivo* MRI, all major internal organ systems can be identified with a high level of confidence (Fig. 8D, E). Such data are of particular interest when respiratory or muscular performance has to be evaluated rapidly and non-invasively using living specimens. Note in particular the difference in contrast within the adductor muscle, which illustrates its bipartite macrostructure divided into smooth (catch) and striated (quick) muscle (Fig. 8D, E). The scan also reveals that a smaller, juvenile specimen is attached to the initially analyzed adult oyster (Fig. 8D).

Scan 17

Eastern oyster, *Crassostrea virginica* (Bivalvia: Ostreidae), adult, 135 mm TL, dataset acquired *in vivo*, scanned in sea water (Table 3). For this particular specimen, a ROI focusing on the viscera was chosen. As a single virtual sagittal section shows, the data permit differentiation of the main muscular and circulatory elements (Fig. 8F).

Scan 18

Great scallop, *Pecten maximus* (Bivalvia: Pectinidae), adult, 99 mm TL, dataset acquired *in vivo*, scanned in sea water (Table 3). A virtual sagittal section shows that similar to the scans performed on living specimens of the bivalve species *M. edulis* (scan 12), *O. edulis* (scan 16), and *C. virginica* (scan 17) all major internal organ systems can be recognized (Fig. 8G). Particularly conspicuous are the digestive gland, kidney, gills, and adductor muscle. In addition, the shape of the mineralized valves can be ascertained due to the positive contrast provided by the signal-emitting liquid (*i.e.,* sea water) surrounding these structures. However, these *in vivo* MRI data show more movement artifacts around the gills than in the oyster datasets due to a generally increased water circulation inside scallops.

Scan 19

Common cuttlefish, *Sepia officinalis* (Cephalopoda: Sepiidae), sub-adult, 37 mm TL, formalin-fixed, ethanol-preserved, dataset acquired *ex vivo*, scanned in distilled water (Table 3). A virtual horizontal section shows that cephalopod internal anatomy can be visualized at a high level of confidence using preclinical MRI (Fig. 8H). Prominent internal structures that can be identified are the digestive gland, ink sac, optic lobes, buccal mass, and statocysts, while external structures such as suckers or the muscular mantle can be seen as well. In addition, smaller anatomical structures like the lacunae or individual components of the statocysts can be differentiated as well. These structures can also be seen in arbitrary 2D sections through the 3D dataset, here shown in the form of a false-colored composite image of a horizontal, sagittal, and transverse section (Fig. 8I).

Scan 20

Ram's horn squid, *Spirula spirula* (Cephalopoda: Spirulidae), adult, 55 mm TL, formalin-fixed, ethanol-preserved, dataset acquired *ex vivo*, scanned in distilled water (Table 3). As virtual horizontal and transverse sections through the MRI dataset illustrate, various internal organs can be identified in this specimen. For example, due to the divergent contrast properties of the constituent as well as the surrounding tissues, arm nerves or the esophagus can be readily singled out (Fig. 9A, B). For segmentation and subsequent 3D modeling purposes, the 2D dataset was zero-filled to 60 μm along the Z axis. As an oblique anterodorsal view of the resulting 3D model shows, segmentation of complex MRI datasets can be used to single out individual structures for their more informative presentation in a didactical sense (Fig. 9C).

Scan 21

Common cuttlefish, *Sepia officinalis* (Cephalopoda: Sepiidae), sub-adult, 37 mm TL, formalin-fixed, ethanol-preserved, dataset acquired *ex vivo*, scanned in distilled water (Table 3). This 2D scan was made to obtain a morphological reference dataset for the subsequently conducted DTI scan (see below). As was the case for all previous MRI scans of cephalopods (Figs. 8H, 9A), the acquired data permit rapid differentiation of major internal and external structures (Fig. 9D).

Scan 22

Common cuttlefish, *Sepia officinalis* (Cephalopoda: Sepiidae), sub-adult, 37 mm TL, formalin-fixed, ethanol-preserved, dataset acquired *ex vivo*, scanned in distilled water (Table 3). As a proof-of-principle for the application of DTI in malacological research, brain and optic lobes were selected for fiber tract visualization in a cuttlefish. To this end, a ROI comprising the head was chosen (Fig. 9E). The data show that diffusion along fiber tracts is still present *post mortem* (Fig. 9F) and that density of the fiber tracts is significantly higher in the optic lobes than in the brain (Fig. 9G).

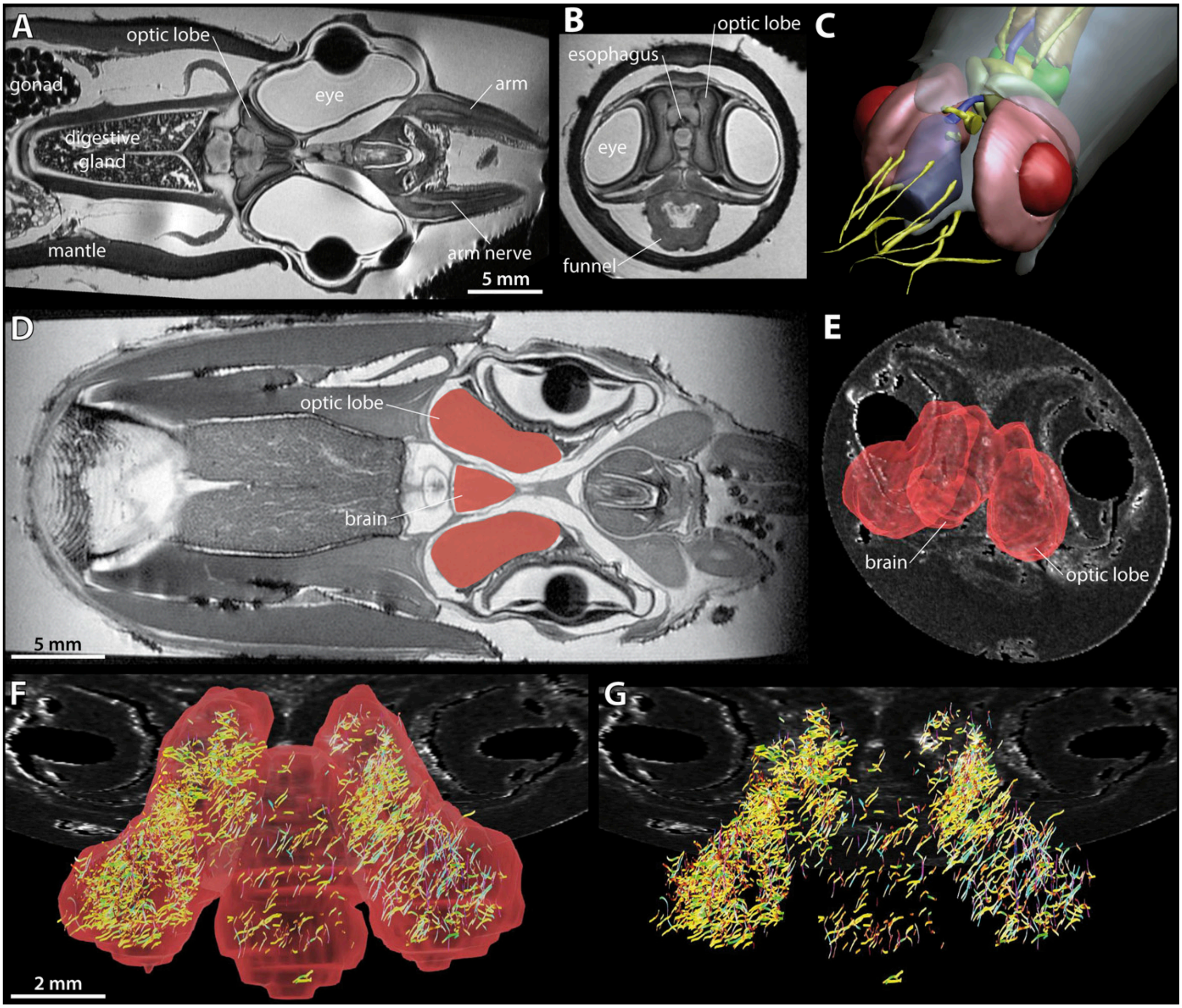

Figure 9. Magnetic resonance imaging data of adult specimens of the cephalopods *Spirula spirula* (A-C) and *Sepia officinalis* (D-G) obtained using high-field preclinical scanning systems. A. Virtual horizontal section, anterior to right. B. Virtual transverse section. C. Solid and semi-transparent surface rendering of segmented structures, oblique anterodorsal view. Blue = digestive tract, brown = digestive gland, green = statocysts, grey = mantle, red = eyes, yellow = nervous system. D. Virtual horizontal section at the level of the optic lobes, anterior to right. Areas selected for visualization by diffusion tensor imaging segmented in red. E. Semi-transparent volume rendering of the areas segmented as in D. shown in combination with a virtual transverse section at the level of the lenses, oblique posterodorsal view. F, G. Diffusion tensor imaging data showing fiber tract orientation in optic lobes and the brain, dorsal view. All renderings and virtual sections created using the free software Fiji (A, B, D), Acrobat Reader (C), and DSI Studio (E-G) at 30 µm isotropic (A-C), 30 x 30 x 100 µm (D), and 58.6 x 58.6 x 235 µm (E-G) voxel resolution.

Clinical magnetic resonance imaging

Scan 23

Oman cuttlefish, *Sepia omani* (Cephalopoda: Sepiidae), adult, 247 mm TL, formalin-fixed, ethanol-preserved, dataset acquired *ex vivo*, scanned in air (Table 3). This particular specimen was removed from its ethanol-filled container, rinsed, and placed inside an air-filled glass jar that was sealed prior to positioning inside the MRI coil. Using this experimental setup, the evaporation of the ethanol still contained within the sample's tissues led to an alcohol-saturated atmosphere inside the glass jar, effectively preventing specimen

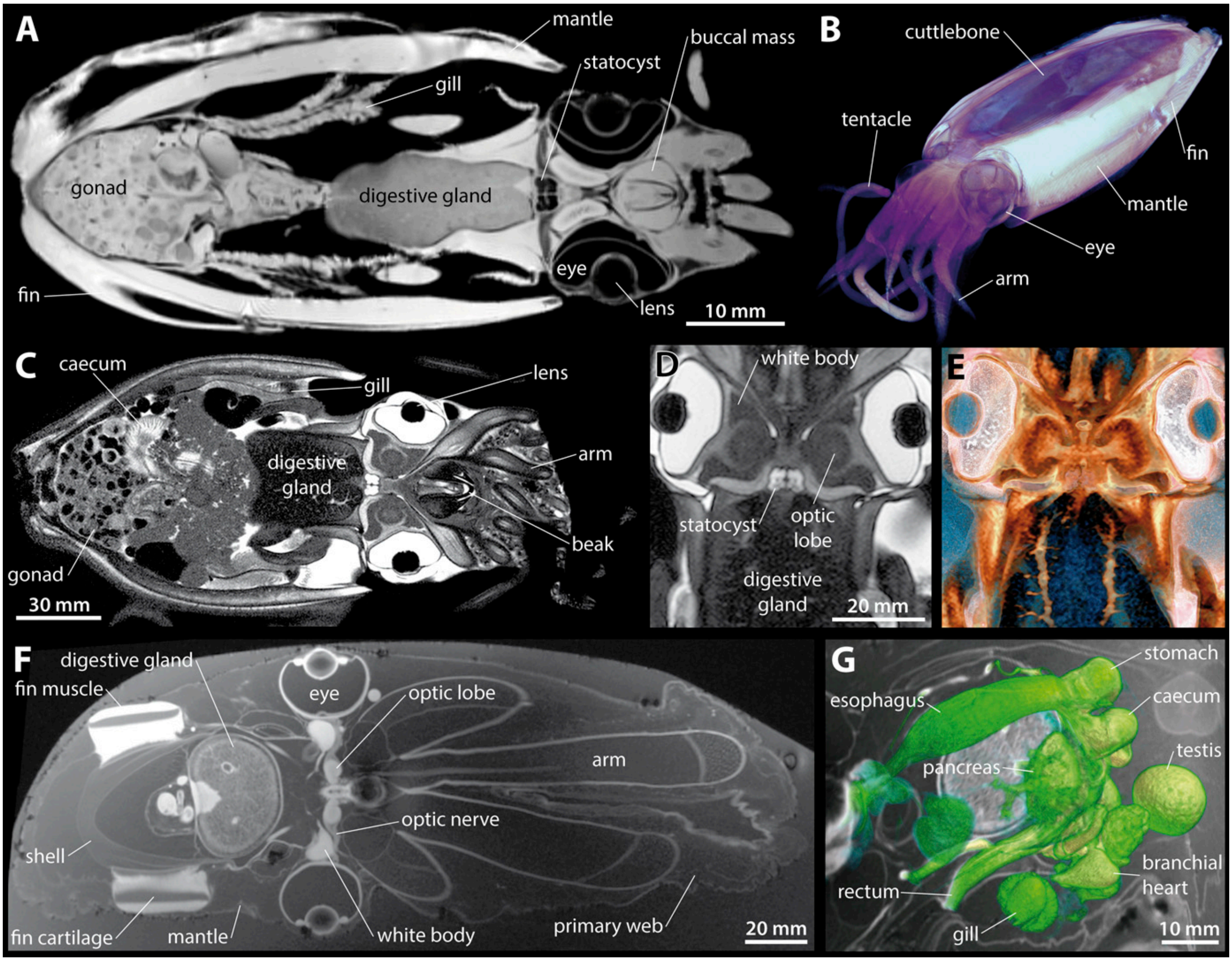

Figure 10. Magnetic resonance imaging data of adult specimens of the cephalopods *Sepia omani* (A, B), *Sepia officinalis* (C-E), and *Grimpoteuthis* sp. (F, G) obtained using high-field clinical scanning systems. A. Virtual horizontal section at the level of the statocyst, anterior to right. B. Semi-transparent volume rendering, oblique anterodorsal view. C. Virtual horizontal section at the level of the digestive gland, anterior facing right. D. Virtual horizontal section at the level of the eyes, anterior facing up. E. Semi-transparent volume rendering, dorsal view. F. Virtual horizontal section at the level of the optic lobes, anterior to right. G. Solid volume rendering of selected internal organs combined with a virtual sagittal section, oblique anterodorsal view. All renderings and virtual sections created using the commercial software Amira (A, B, F, G), the free software Fiji (C), and the proprietary scanner software syngo (D, E) at 173.5 µm isotropic (A, B), 200 x 200 x 1,000 µm (C), 117 µm isotropic (D, E), and 140 µm isotropic (F, G) voxel resolution.

movement as a result of desiccation during the scan. In addition, structural integrity of the animal during the scan was ensured due to the rubber-like properties of its formalin-fixed and long-term ethanol-preserved soft tissues. A virtual horizontal section at the level of the eyes shows that various external and internal structures can be differentiated, including the mantle, gonad, digestive gland, gills, statocysts, lenses, and buccal mass (Fig. 10A). Due to the specimen being surrounded by air, the strong contrast between the object and the surrounding medium results in the possibility to obtain informative volume rendering data of the entire specimen without the need for manual segmentation of individual structures (Fig. 10B).

Scan 24

Common cuttlefish, *Sepia officinalis* (Cephalopoda: Sepiidae), adult, 341 mm TL, dataset acquired *in vivo*, scanned partially immersed in sea water (Table 3). As a virtual horizontal section shows, these rapidly generated 2D MRI data permit differentiation of all major internal organ systems, including the gonads, components of the digestive tract, gills, eyes, and lenses (Fig. 10C). In addition, mineralized and therefore *per se* not very MRI-signal-intense structures such as the lower and upper beak or lenses become apparent as well due to being surrounded by tissues rich in signal-emitting water molecules. A direct comparison with the data from the fixed specimen of *S. omani* shown in the previous scan (Fig. 10A) illustrates a considerable degree of distortion that specific cephalopod organs may undergo during fixation and subsequent long-term storage in ethanol.

Scan 25

Common cuttlefish, *Sepia officinalis* (Cephalopoda: Sepiidae), adult, 341 mm TL, dataset acquired *in vivo*, scanned partially immersed in sea water (Table 3). The living, adult specimen of *S. officinalis* introduced in the previous scan was analyzed again during the same imaging session using a ROI focusing on the specimen's head. A virtual horizontal section illustrates that the resulting data permit differentiating white bodies from the optic lobes as well as selected internal elements of the statocysts (Fig. 10D). Due to the 3D nature of the acquired dataset, volume rendering allows obtaining a more plastic impression of the structural composition of the specimen's head (Fig. 10E).

Scan 26

Dumbo octopus, *Grimpoteuthis* sp. (Cephalopoda: Grimpoteuthidae), adult, 290 mm TL, formalin-fixed, formalin-preserved, dataset acquired *ex vivo*, scanned in formalin (Table 3). This intact cirrate specimen was collected during a scientific cruise in the Northern Pacific Ocean (Werner *et al.* 2016). As a virtual horizontal section shows, all internal structures relevant for the identification of a dumbo octopus to species level can be differentiated (Fig. 10F). These structures include, among others, digestive tract, central nervous system with optic lobes and nerves, white bodies, arms, web, fins and their muscles, as well as eyes. All of these organs are suitable for 3D reconstruction using manual segmentation followed by surface rendering. In addition, a volume rendering of selected internal organs reveals further structures that can be visualized in 3D, including the gills, branchial hearts, as well as all major components of the digestive tract such as esophagus, stomach, caecum, and rectum (Fig. 10G). The presence of a large testis shows that the captured animal is an adult male (Fig. 10G). In contrast to the previous two cephalopod specimens analyzed using clinical MRI (scans 23-25), this sample was scanned fully immersed in a liquid rich in MRI-signal-emitting water molecules (*i.e.,* formalin), which complicates threshold-based volume rendering due to the absence of a sharp boundary between specimen and surrounding medium.

DISCUSSION

Due the large amounts of informative data that can be rapidly generated using genomic tools, classical morphological techniques such as dissection, histology, or electron microscopy are gradually being replaced (Giribet 2010, Giribet 2015). However, as illustrated in the present as well as previous studies, 3D imaging techniques provide rapid access to complex anatomical features, thereby allowing large-scale comparative analyses within and across taxa. In order to correlate genotype with phenotype at the desired large scale, such digital imaging techniques should be applied more broadly in zoological research (Ziegler *et al.* 2010). Due to their 3D nature, these data permit the simultaneous virtual dissection of scanned specimens (Ziegler and Menze 2013), ultimately triggering new findings that lead to hypotheses on molluscan form, function, and evolution. However, presumably the greatest asset of a digital approach is the possibility to deposit large amounts of structural data in online repositories (Berquist *et al.* 2012, Lenihan *et al.* 2014, Ziegler *et al.* 2014), thus significantly increasing data transparency and permitting future data mining. Because the concept of "big data" analysis is now also progressing into structural organismic research, high-throughput imaging and segmentation protocols from large-scale preclinical or clinical studies (Akselrod-Ballin *et al.* 2016) can be expected to significantly contribute to tomography-based studies in zoological disciplines, including malacology.

Computed tomography techniques in malacological research

μCT

As demonstrated here, X-ray-based techniques are particularly suited for the rapid visualization of molluscan hard part morphology in 3D, including spicules, radula, and ligament, but in particular aspects of the macro- and microstructure of the molluscan shell (Figs. 1-3). The possibility to generate such data using μCT had already been noticed more than a decade ago (Vendrasco *et al.* 2004). Consequently, molluscs are increasingly being analyzed using this technique, although so far primarily in studies focusing on selected aspects of shell and spicule morphology (Ruthensteiner *et al.* 2010, Alba-Tercedor and Sánchez-Tocino 2011, Connors *et al.* 2012, Lukeneder 2012, Sutton and Sigwart 2012, Ziegler and Menze 2013, Liew *et al.* 2014, Jochum *et al.* 2014, Noshita 2014, Hoffmann *et al.* 2015, Jochum *et al.* 2015, Vinther 2015, Xavier *et al.* 2015, Becker *et al.* 2016, Liew and Schilthuizen 2016, Cotton *et al.* 2017, Jochum *et al.* 2017, Sumner-Rooney and Sigwart 2017). But, μCT has also been used in experimental malacological research, for example in studies on burrow systems of wood-boring bivalves (Amon *et al.* 2015) or of a sediment-boring gastropod (Hale *et al.* 2015) as well as on the effects of ocean acidification on calcified structures in selected conchiferans (Keklikoglou *et al.* 2015, Chatzinikolaou *et al.* 2017, Howes *et al.* 2017). In addition, this X-ray-based imaging technique was employed to study functional and biomechanical aspects of molluscs, including the microstructure of the byssus (Frølich *et al.* 2015), eye anatomy in a chiton (Li *et al.* 2015) as well as in a bivalve (Palmer *et al.* 2017), and radular tooth morphology in a chiton (Ukmar-Godec *et al.* 2015). Recently, µCT systems of the latest generation are being used to study early ontogenetic stages of molluscs, for example in attempts to understand shell growth or the formation of suture patterns (Inoue and Kondo 2016, Lemanis *et al.* 2016, Noshita *et al.* 2016).

However, the relatively weak performance of X-ray tubes even in modern µCT systems means that scans at voxel resolutions in the nanometer scale will take significantly longer than scans with similar parameters conducted using SRµCT beamlines. For specific studies it might therefore be of interest to obtain scan time at one of these facilities. Compared to µCT scanners, SRµCT beamlines offer improved physical properties and are usually equipped with robotic sample holders that enable high-throughput scanning. However, a notable caveat of such analyses is the high potential for irreversible damage to the specimen's DNA, a consequence of the high X-ray doses emitted on SRµCT systems (Immel *et al.* 2016). Significantly less damage to DNA can be observed when conventional µCT or CT systems are used (Paredes *et al.* 2012, Hall *et al.* 2015, Immel *et al.* 2016, Wanek and Rühli 2016). In addition, due to technical limitations SRµCT is commonly performed using a FOV of only a few millimeters width and height (Zanette *et al.* 2014), which obviously complicates the analysis of larger specimens. One example for SRµCT-based research on molluscs is provided by a study focusing on embryonic shell formation in a gastropod (Marxen *et al.* 2008).

CT

CT was here performed using a system originally designed for human diagnostics. The scan of an adult specimen of the relatively large cephalopod *Dosidicus gigas* provides only a limited degree of soft tissue contrast (Fig. 4) if compared with results on *Sepia omani* derived from clinical MRI (Fig. 10A, B). However, the specific CT scanner settings used here still permit differentiation of selected internal soft and hard parts like the digestive gland (Fig. 4B) or ink sac and gladius (Fig. 4D), in addition to information about the exterior shape (Fig. 4C). Therefore, despite its limited application in malacological research so far, CT must be seen as an imaging modality that may provide a significant amount of valuable morphological data on larger molluscs, in particular when scanning systems of the latest generation are employed. Prominent examples for such modern CT scanners are interventional angiography systems used in human diagnostics, primarily during surgery. These scanners have a smaller FOV (*e.g.,* 30 x 30 cm) than conventional CT systems, but can acquire 3D datasets at a relatively high IVR (*e.g.,* 150-500 µm) in less than a minute.

Contrast-enhanced µCT

The µCT and CT scans presented here show that the attenuation contrast typically employed in X-ray-based imaging yields data primarily restricted to hard parts, even in the presence of large amounts of soft tissues (Fig. 1, Fig. 3A-D). Nevertheless, soft part contrast can be obtained using such techniques, but the soft tissues of the specimen under study need to be enriched with an X-ray-dense contrast agent (Metscher 2009, Pauwels *et al.* 2013). In the present study, PTA was chosen for contrast-enhanced µCT, because this chemical offers excellent contrast properties. However, PTA exhibits only a relatively slow diffusion presumably due to the large size of the compound. PTA was previously estimated to penetrate earth worm tissues at about 1 mm per week, but this parameter may depend on various chemical and physical properties of the specific tissues involved (Fernández *et al.* 2014). The results obtained here illustrate that PTA is a suitable contrast agent for molluscan specimens and can – given sufficient diffusion time and initial concentration – penetrate even thick tissues, as shown here by the successful staining of the foot of a chiton (Fig. 5A-C) and the mantle of a cephalopod (Fig. 5D-G). In contrast, smaller specimens with less dense tissues such as the cephalopod embryo analyzed here (Fig. 6) will stain rapidly. Prominent alternatives to PTA are the various compounds containing iodine (Metscher 2009, Pauwels *et al.* 2013, Gignac *et al.* 2016), but care needs to be taken when using these chemicals as they have been shown to lead to significant specimen shrinkage as well as overstaining under certain conditions (Vickerton *et al.* 2013, Buytaert *et al.* 2014, Gignac and Kley 2014, Li *et al.* 2015, Sombke *et al.* 2015, Li *et al.* 2016, Hedrick *et al.* 2018).

With regard to their usefulness in contrast-enhanced µCT, common to all staining agents mentioned above is that they do not display any form of specific staining properties (Metscher 2009, Pauwels *et al.* 2013, Gignac *et al.* 2016). However, although not a specific stain *per se*, certain contrast preferences of PTA have been documented in the past during studies aimed at using this agent in ultrastructural analyses (Quintarelli *et al.* 1971, 1973). However, the specific staining properties of PTA pale in comparison to established histological stains such as hematoxylin and eosin, Azan, or Mallory's trichrome. This important fact must be kept in mind when analyzing data derived from contrast-enhanced µCT experiments, because the resulting grey-scale images require a profound knowledge of molluscan anatomy to avoid misinterpretations. One way to facilitate the identification of different structures of complex µCT datasets is to apply dual-energy CT methods (Handschuh *et al.* 2017).

Studies that previously have analyzed molluscan taxa using contrast-enhanced µCT comprise experiments on the general suitability of all higher molluscan taxa for this approach using different contrast agents (Golding and Jones 2007, Faulwetter *et al.* 2012, Cándas *et al.* 2015, Faulwetter *et al.* 2015, Cándas *et al.* 2016). In addition, more specific studies have focused on odontophoral cartilage morphology in selected gastropods (Golding *et al.* 2009), changes in ganglionic system anatomy during cephalopod ontogeny (Kerbl *et al.* 2013), the internal anatomy of a larval cephalopod (Xavier *et al.* 2015), the reproductive system of a nudibranch (Cándas *et al.* 2017), the anatomy of Hoyle's organ in a cephalopod (Cyran *et al.* 2018), or the visualization of internal and external organs of selected gastropod species (Pedrouzo *et al.* 2018). Furthermore, contrast-enhanced µCT was performed in a methodological study on correlative imaging using a bivalve (Handschuh *et al.* 2013), to describe several new nudibranch species (Moles *et al.* 2016, Moles *et al.* 2017), and to illustrate the internal anatomy of numerous bivalve species (Machado *et al.* 2018).

As outlined above, contrast-enhanced µCT involves penetration of the specimen by an X-ray-dense contrast agent, thus altering the object under study. While such an approach may be applicable for certain samples, it constitutes an interference with the specimen's integrity. This will in principle render this protocol impractical for use on rare or otherwise valuable specimens, *e.g.*, type material. However, initial results from a limited number of studies suggest that stain removal could be possible under certain conditions (Schmidbaur *et al.* 2015, Gignac *et al.* 2016). An entirely non-invasive alternative to contrast-enhanced µCT is phase contrast imaging. This modality involves technical adjustments to attenuation contrast-based SRµCT beamlines (Zehbe *et al.* 2010, Saccomano *et al.* 2018), but lately also to lab-based µCT equipment (Zanette *et al.* 2014). In molluscs, this approach has so far only been used to analyze pearls (Krzemnicki *et al.* 2017), but is bound to develop into a promising technique for malacological research in the near future.

Magnetic resonance imaging techniques in malacological research

Preclinical MRI

As shown in the previous µCT scans, excellent soft part information can be obtained using attenuation contrast-based techniques in combination with staining agents, but this approach may not be applicable in case of all molluscan specimens. As an alternative to this non-destructive, but invasive approach to visualizing molluscan structural detail in 3D, various MRI techniques can be employed. In contrast to µCT or CT, information on molluscan soft parts is usually obtained without the use of contrast agents, thus rendering this approach particularly attractive for the study of type material. In order to achieve high voxel resolutions, preclinical MRI systems are conventionally employed. This approach uses equipment designed for experimental animals such as mice, rats, or smaller primate species (Ziegler *et al.* 2011, Zanette *et al.* 2014). However, these instruments have a limited FOV and are therefore only suitable for specimens on the millimeter and centimeter scale. In addition, due to their lower overall distribution, preclinical MRI systems are usually less accessible than clinical MRI scanners (Ziegler *et al.* 2008). But, in contrast to the latter, there are no restrictions regarding protocol choice on preclinical MRI scanners (see below), although overheating of the gradient system may sometimes lead to an interruption of longer 3D scans (Ziegler *et al.* 2011). In addition, MRI in general shows strong artifacts when zoological specimens are analyzed that contain para- or ferromagnetic substances (Ziegler and Mueller 2011). Prominent examples include ingesta contained within the digestive tract (*e.g.*, in sediment feeders) or the strongly mineralized radula of chitons (Ziegler *et al.* 2011). Despite these caveats, the scans conducted in the present study show that preclinical MRI must be considered as a powerful tool to visualize molluscan internal and external structures at voxel resolutions in the single- to double-digit micrometer scale obtained from uncontrasted millimeter- to centimeter-sized specimens.

Several studies on molluscan specimens have so far been conducted using preclinical MRI, including analyses of the single-cell and sub-cellular composition of neurons from derived taxa (Hsu *et al.* 1996, Grant *et al.* 2000, Gozansky *et al.* 2003, Lee *et al.* 2015), physiological capacities of cephalopods and bivalves measured *in vivo* (Bock *et al.* 2004, Melzner *et al.* 2006, Bock *et al.* 2007, Melzner *et al.* 2007, Lannig *et al.* 2008, Gutowska *et al.* 2010, Lee *et al.* 2010, Seo *et al.* 2014, Sukhotin *et al.* 2017), reproductive organ maturation and sex determination in oysters (Davenel *et al.* 2006, Davenel *et al.* 2010, Smith and Reddy 2012), or visual system anatomy in cephalopods (Jiang *et al.* 2013, Chung and Marshall 2014, Chung and Marshall 2017, Liu *et al.* 2017, Liu *et al.* 2018). In addition, preclinical MRI was applied to study the anatomy of a cobalt-labeled cephalopod brain (Quast *et al.* 2001), to conduct analyses of pathological alterations in belemnites (Mietchen *et al.* 2005, Mietchen *et al.* 2008) and to study the internal anatomy of a gastropod (Ziegler and Mueller 2011). In addition, the brain anatomy of a cephalopod (Solé *et al.* 2013), the morphology and adhesion mechanism of the octopus sucker (Tramacere *et al.* 2013), and the first 3D reconstruction of internal organs in a dumbo octopod hatchling (Shea *et al.* 2018) were performed using preclinical MRI.

With regard to specimen preparation for MRI, it is important to note that MRI protocols in principle permit scanning specimens fully immersed in ethanol (Sigl *et al.* 2013). This may be advantageous for various reasons, for example if the higher surface tension of water leads to air bubbles being trapped inside a specimen, which usually results in the presence of strong susceptibility artifacts (Ziegler *et al.* 2011) or when museum specimens have to be analyzed as non-invasively as feasible. However, the possibility to scan a specimen in ethanol depends on various parameters, in particular magnetic field strength and ethanol concentration. In general, a mix of liquids is problematic for MRI as such a solution may lead to chemical shift artifacts, *e.g.,* between water and ethanol. For these reasons, all specimens analyzed here using preclinical MRI systems were either immersed in distilled water prior to scanning, were kept in their formalin fixative, or were embedded in agarose in order to provide a homogenous medium surrounding the specimen.

Clinical MRI

In contrast to the previous technique, clinical MRI is using scanning systems specifically designed for human diagnostics. Due to their technical optimization for medical examinations of living human subjects, clinical MRI systems usually employ fast scanning sequences, often inhibiting longer protocols with large volume coverage and high voxel resolutions, because such sequences might impact the patient due to rapid gradient switching or the applied radiofrequency power. However, the settings on most clinical MRI systems can be changed by trained personnel to accommodate zoological specimens intended for longer 3D scans. But, as illustrated here (Fig. 10A, B), 2D scanning sequences with resolutions along the Z axis that closely approach those in the X and Y axes (*e.g.,* 500 x 500 x 800 µm) can also be used to obtain valuable structural information from molluscan specimens, whether *in vivo* or *ex vivo.* Clinical MRI studies that have analyzed molluscan taxa in the past include experiments on various morphological and anatomical features of bivalves (Pouvreau *et al.* 2006, Holliman *et al.* 2008, von Brand *et al.* 2009), soft part morphology in a gastropod (Cooper 2011) as well as selected cephalopods (Ziegler and Menze 2013, Xavier *et al.* 2015), the kinematics of buccal mass movement in a gastropod (Neustadter *et al.* 2002, Novakovic *et al.* 2006), and the auditory capacity of a cephalopod (Mooney *et al.* 2010).

Outlook

In addition to a growing number of studies, the data presented here show that 3D imaging techniques such as MRI or CT can be used to gather structural information from a diverse array of molluscan specimens rapidly, non-destructively or even entirely non-invasively, and in digital form. As illustrated by the first reconstruction of the internal anatomy of a deep sea incirrate embryo presented here, 3D imaging techniques are capable of providing new analytical pathways for malacological research that are bound to lead to discoveries that would have been impossible using conventional morphological techniques. Furthermore, digital 3D datasets can be distributed through online repositories and used for various downstream analyses such as correlative imaging, pattern recognition, and shape analysis as well as in morphometric or volumetric studies. Foreseeable technical improvements such as robotic high-throughput scanning, significantly improved voxel resolution, or specific staining protocols are bound to lead to a significant extension of the methodological spectrum available to malacologists.

ACKNOWLEDGEMENTS

We would like to express our gratitude to Adam J. Baldinger, Thomas Bartolomaeus, Patrick Beckers, Rüdiger Bieler, Roger T. Hanlon, Carsten Lüter, Iliana Ruiz-Cooley, Tom Schiøtte, Andreas Schmidt-Rhaesa, and Sid Staubach for help with specimen collection or for providing access to museum material. Cornelius Faber, Julia Koch, Tony Stöcker, and W. Caroline West kindly facilitated use of scanning systems. We would also like to thank Julie Arruda, Scott Cramer, Jörg Döpfert, Charlotte Eymann, Bastian Maus, Malte Ogurreck, Christina L. Sagorny, Gillian Trombke, and Christopher Witte for support with data acquisition and analysis. We are particularly grateful to Elizabeth K. Shea for inviting the present contribution and for her extensive commentary on the manuscript. We also thank two anonymous reviewers for their helpful criticisms. Funding for this study was provided by the Ocean Life Institute, the Office of Naval Research, the Seaver Institute, and the Deutsche Forschungsgemeinschaft (INST 217/849-1 FUGG).

LITERATURE CITED

Aguilera, F., C. McDougall, and B. M. Degnan. 2017. Co-option and de novo gene evolution underlie molluscan shell diversity. *Molecular Biology and Evolution* **34:** 779–792.

Akselrod-Ballin, A., H. Dafni, Y. Addadi, I. Biton, R. Avni, Y. Brenner, and M. Neeman. 2016. Multimodal correlative preclinical whole body imaging and segmentation. *Scientific Reports* **6:** 27940.

Alba-Tercedor, J. and L. Sánchez-Tocino. 2011. The use of the SkyScan 1172 high-resolution micro-CT to elucidate if the spicules of the "sea slugs" (Mollusca: Nudibranchia, Opisthobranchia) have a structural or a defensive function. *In*: Micro-CT 2011 User Meeting Abstract Book. Pp. 113–114.

Altenberg, L. 2005. Modularity in evolution: Some low-level questions. *In*: W. Callebaut and D. Rasskin-Gutman, eds., *Modularity: Understanding the Development and Evolution of Complex Natural Systems*. MIT Press, Cambridge, Massachusetts. Pp. 99–128.

Amon, D. J., D. Sykes, F. Ahmed, J. T. Copley, K. M. Kemp, P. A. Tyler, C. M. Young, and A. G. Glover. 2015. Burrow forms, growth rates and feeding rates of wood-boring Xylophagaidae bivalves revealed by micro-computed tomography. *Frontiers in Marine Science* **2:** 10.

Becker, M., S. Zielske, and M. Haase. 2016. Conflict of mitochondrial phylogeny and morphology-based classification in a pair of freshwater gastropods (Caenogastropoda, Truncatelloidea, Tateidae) from New Caledonia. *ZooKeys* **603:** 17–32.

Berquist, R. M., K. M. Gledhill, M. W. Peterson, A. H. Doan, G. T. Baxter, K. E. Yopak, N. Kang, H. J. Walker, P. A. Hastings, and L. R. Frank. 2012. The Digital Fish Library: Using MRI to digitize, database, and document the morphological diversity of fish. *PLoS ONE* **7**: e34499.

Bock, C., G. Lurman, and H.-O. Pörtner. 2007. Temperature and oxygenation dependence of haemoglobin and hemocyanin relaxation times at 9.4T. *Proceedings of the International Society for Magnetic Resonance in Medicine* **15:** 2749.

Bock, C., S. Schmidt, F. Melzner, and H.-O. Poertner. 2004. Hypoxia induced changes in the brain of hypoxic tolerant cuttlefish *Sepia officinalis*. *Proceedings of the International Society for Magnetic Resonance in Medicine* **11:** 1455.

Boistel, R., J. Swoger, U. Kržič, V. Fernandez, B. Gillet, and E. G. Reynaud. 2011. The future of three-dimensional microscopic imaging in marine biology. *Marine Ecology* **32:** 438–452.

Boyle, P. R. 2010. Cephalopods. *In*: R. Hubrecht and J. Kirkwood, eds., *The UFAW Handbook on the Care and Management of Laboratory and Other Research Animals. 8th edition*. Wiley-Blackwell, Chichester. Pp. 794–817.

Budelmann, B. U. 2010. Cephalopoda. *In*: R. Hubrecht and J. Kirkwood, eds., *The UFAW Handbook on the Care and Management of Laboratory and Other Research Animals. 8th edition*. Wiley-Blackwell, Chichester. Pp. 787–793.

Buytaert, J., J. Goyens, D. De Greef, P. Aerts, and H. Dirckx. 2014. Volume shrinkage of bone, brain and muscle tissue in sample preparation for micro-CT and light sheet fluorescence microscopy (LSFM). *Microscopy and Microanalysis* **20:** 1208–1217.

Candás, M., G. Díaz-Agras, M. Abad, L. Barrio, X. Cunha, L. Pedrouzo, M. P. Senarís, Ó. García-Álvarez, and V. Urgorri. 2015. Application of microCT in the study of the anatomy of small marine molluscs. *In*: Micro-CT 2015 User Meeting Abstract Book. Pp. 93–97.

Candás, M., G. Díaz-Agras, M. Abad, L. Barrio, X. Cunha, L. Pedrouzo, M. P. Senaris, Ó. García-Álvarez, and V. Urgorri. 2016. Application of microCT in the study of the anatomy of small marine molluscs. *Microscopy and Analysis* **30:** S8–S11.

Candás, M., G. Díaz-Agras, and V. Urgorri. 2017. First steps in morphological analysis of the reproductive system of *Doto pinnatifida* (Montagu, 1804). *In*: Micro-CT 2017 User Meeting Abstract Book. Pp. 112–116.

Chatzinikolaou, E., P. Grigoriou, K. Kelikoglou, S. Faulwetter, and N. Papageorgiou. 2017. The combined effects of reduced pH and elevated temperature on the shell density of two gastropod species measured using micro-CT imaging. *ICES Journal of Marine Science* **74:** 1135–1149.

Chughtai, K., Y. Song, P. Zhang, B. Derstine, E. Gatza, J. Friedman, L. Hully, C. Inglis, S. Goldstein, J. Magenau, A. Pawarode, P. Reddy, M. Riwes, G. Yanik, S. C. Wang, and S. W. Choi. 2016. Analytic morphomics: A novel CT imaging approach to quantify adipose tissue and muscle composition in allogeneic hematopoietic cell transplantation. *Bone Marrow Transplantation* **51:** 446–450.

Chung, W. S. and J. Marshall. 2014. Range-finding in squid using retinal deformation and image blur. *Current Biology* **24:** R64–R65.

Chung, W. S. and N. J. Marshall. 2017. Complex visual adaptations in squid for specific tasks in different environments. *Frontiers in Physiology* **8:** 105.

Connors, M. J., H. Ehrlich, M. Hog, C. Godeffroy, S. Araya, I. Kallai, D. Gazit, M. Boyce, and C. Ortiz. 2012. Three-dimensional structure of the shell plate assembly of the chiton *Tonicella marmorea* and its biomechanical consequences. *Journal of Structural Biology* **177:** 314–328.

Cooper, J. E. 2011. Anesthesia, analgesia, and euthanasia of invertebrates. *ILAR Journal* **52:** 196–204.

Cotton, L. J., A. W. Jansten, P. N. Pearson, and R. van Driel. 2017. Pteropoda (Mollusca, Gastropoda, Thecosomata) from the Eocene/Oligocene boundary interval of three cored boreholes in southern coastal Tanzania and their response to the global cooling event. *Palaeontologia Electronica* **20.3.52A:** 1–21.

Cyran, N., A. Palumbo, W. Klepal, E. A. G. Vidal, Y. Staedler, J. Schönenberger, and J. von Byern. 2018. The short life of the Hoyle organ of *Sepia officinalis*: Formation, differentiation and degradation by programmed cell death. *Hydrobiologia* **808:** 35–55.

Davenel, A., R. González, M. Suquet, S. Quellec, and R. Robert. 2010. Individual monitoring of gonad development in the European flat oyster *Ostrea edulis* by in vivo magnetic resonance imaging. *Aquaculture* **307:** 165–169.

Davenel, A., S. Quellec, and S. Pouvreau. 2006. Noninvasive characterization of gonad maturation and determination of the sex of Pacific oysters by MRI. *Magnetic Resonance Imaging* **24:** 1103–1110.

Dunn, C. W., G. Giribet, G. D. Edgecombe, and A. Hejnol. 2014. Animal phylogeny and its evolutionary implications. *Annual Review of Ecology, Evolution, and Systematics* **45:** 371–395.

Faulwetter, S., N. Minadakis, K. Keklikoglou, M. Doerr, and C. Arvanitidis. 2015. First steps towards the development of an integrated metadata management system for biodiversity-related micro-CT datasets. *In*: Micro-CT 2015 User Meeting Abstract Book. Pp. 142–155.

Faulwetter, S., D. Thanos, V. Aikaterini, and A. Christos. 2012. Investigation of contrast enhancing techniques for the application of micro-CT in marine biodiversity studies. *In*: Micro-CT 2012 User Meeting Abstract Book. Pp. 12–20.

Fernández, R., S. Kvist, J. Lenihan, G. Giribet, and A. Ziegler. 2014. *Sine systemate chaos?* A versatile tool for earthworm taxonomy: Non-destructive imaging of freshly fixed and museum specimens using micro-computed tomography. *PLoS ONE* **9:** e96617.

Frølich, S., H. Leemreize, J. S. Thomsen, and H. Birkedal. 2015. Pore structures in the biomineralized byssus of *Anomia simplex*. *Key Engineering Materials* **672:** 71–79.

Furbank, R. T. and M. Tester. 2011. Phenomics – technologies to relieve the phenotyping bottleneck. *Trends in Plant Science* **16:** 635–644.

Gerlai, R. 2002. Phenomics: fiction or the future? *Trends in Neurosciences* **25:** 506–509.

Gignac, P. M. and N. J. Kley. 2014. Iodine-enhanced micro-CT imaging: Methodological refinements for the study of the soft-tissue anatomy of post-embryonic vertebrates. *Journal of Experimental Zoology B (Molecular and Developmental Evolution)* **322:** 166–176.

Gignac, P. M., N. J. Kley, J. A. Clarke, M. W. Colbert, A. C. Morhardt, D. Cerio, I. N. Cost, P. G. Cox, J. D. Daza, C. M. Early, M. S. Echols, R. M. Henkelman, A. N. Herdina, C. M. Holliday, Z. Li, K. Mahlow, S. Merchant, J. Müller, C. P. Orsbon, D. J. Paluh, M. L. Thies, H. P. Tsai, and L. M. Witmer. 2016. Diffusible iodine-based contrast-enhanced computed tomography (diceCT): An emerging tool for rapid, high-resolution, 3-D imaging of metazoan soft tissues. *Journal of Anatomy* **228:** 889–909.

Giribet, G. 2008. Assembling the lophotrochozoan (=spiralian) tree of life. *Philosophical Transactions of the Royal Society B* **363**: 1513–1522.

Giribet, G. 2010. A new dimension in combining data? The use of morphology and phylogenomic data in metazoan systematics. *Acta Zoologica* **91:** 11–19.

Giribet, G. 2015. Morphology should not be forgotten in the era of genomics – a phylogenetic perspective. *Zoologischer Anzeiger* **256:** 96–103.

Giribet, G. 2016. New animal phylogeny: Future challenges for animal phylogeny in the age of phylogenomics. *Organisms Diversity & Evolution* **16:** 419–426.

Golding, R. E. and A. S. Jones. 2007. Micro-CT as a novel technique for 3D reconstruction of molluscan anatomy. *Molluscan Research* **27:** 123–128.

Golding, R. E., W. F. Ponder, and M. Byrne. 2009. Three-dimensional reconstruction of the odontophoral cartilages of Caenogastropoda (Mollusca: Gastropoda) using micro-CT: Morphology and phylogenetic significance. *Journal of Morphology* **270:** 558–587.

Gozansky, E. K., E. L. Ezell, B. U. Budelmann, and M. J. Quast. 2003. Magnetic resonance histology: In situ single cell imaging of receptor cells in an invertebrate (*Lolliguncula brevis*, Cephalopoda) sense organ. *Magnetic Resonance Imaging* **21:** 1019–1022.

Grant, C. U. R., N. R. Aiken, H. D. Plant, S. Gibbs, T. H. Mareci, A. G. Webb, and S. J. Blackband. 2000. NMR spectroscopy of single neurons. *Magnetic Resonance in Medicine* **44:** 19–22.

Gutiérrez, Y., D. Ott, M. Töpperwien, T. Salditt, and C. Scherber. 2018. X-ray computed tomography and its potential in ecological research: A review of studies and optimization of specimen preparation. *Ecology and Evolution* **8:** 7717–7732.

Gutowska, M. A., F. Melzner, M. Langenbuch, C. Bock, G. Claireaux, and H.-O. Pörtner. 2010. Acid-base regulatory ability of the cephalopod (*Sepia officinalis*) in response to environmental hypercapnia. *Journal of Comparative Physiology B* **180:** 323–335.

Hale, R., R. Boardman, M. N. Mavrogordato, I. Sinclair, T. J. Tolhurst, and M. Solan. 2015. High-resolution computed tomography reconstructions of invertebrate burrow systems. *Scientific Data* **2:** 150052.

Hall, A. C., E. Sherlock, and D. Sykes. 2015. Does micro-CT scanning damage DNA in museum specimens? *Journal of Natural Science Collections* **2:** 22–28.

Handschuh, S., N. Baeumler, T. Schwaha, and B. Ruthensteiner. 2013. A correlative approach for combining microCT, light and transmission electron microscopy in a single 3D scenario. *Frontiers in Zoology* **10:** 44.

Handschuh, S., C. J. Beister, B. Ruthensteiner, and B. D. Metscher. 2017. Microscopic dual-energy CT (microDECT): A flexible tool for multichannel *ex vivo* 3D imaging of biological specimens. *Journal of Microscopy* **267:** 3–26.

Hedrick, B. P., L. Yohe, A. Vander Linden, L. M. Dávalos, K. Sears, A. Sadier, S. J. Rossiter, K. T. J. Davies, and E. Dumont. 2018. Assessing soft-tissue shrinkage estimates in museum specimens imaged with diffusible iodine-based contrast-enhanced computed tomography (diceCT). *Microscopy and Microanalysis* **24:** 284–291.

Hoffmann, R., D. Reinhoff, and R. Lemanis. 2015. Non-invasive imaging techniques combined with morphometry: A case study from *Spirula*. *Swiss Journal of Palaeontology* **134:** 207–216.

Hoffmann, R., J. A. Schultz, R. Schellhorn, E. Rybacki, H. Keupp, S. R. Garden, R. Lemanis, and S. Zachow. 2014. Non-invasive imaging methods applied to neo- and paleo-ontological cephalopod research. *Biogeosciences* **11:** 2721–2739.

Holliman, F. M., D. Davis, A. E. Bogan, T. J. Kwak, W. G. Cope, and J. F. Levine. 2008. Magnetic resonance imaging of live freshwater mussels (Unionidae). *Invertebrate Biology* **127:** 396–402.

Houle, D. 2010. Numbering the hairs on our heads: The shared challenge and promise of phenomics. *Proceedings of the National Academy of Sciences* **107:** 1793–1799.

Howes, E. L., R. A. Eagle, J. P. Gattuso, and J. Bijma. 2017. Comparison of Mediterranean pteropod shell biometrics and ultrastructure from historical (1910 and 1921) and present day (2012) samples provides baseline for monitoring effects of global change. *PLoS ONE* **12:** e0167891.

Hsu, E. W., N. R. Aiken, and S. J. Blackband. 1996. Nuclear magnetic resonance microscopy of single neurons under hypotonic perturbation. *American Journal of Physiology* **271:** C1895–C1900.

Immel, A., A. Le Cabec, M. Bonazzi, A. Herbig, H. Temming, V. J. Schuenemann, K. I. Bos, F. Langbein, K. Harvati, A. Bridault, G. Pion, M.-A. Julien, O. Krotova, N. J. Conard, S. C. Münzel, D. G. Drucker, B. Viola, J.-J. Hublin, P. Tafforeau, and J. Krause. Effect of X-ray irradiation on ancient DNA in sub-fossil bones – guidelines for safe X-ray imaging. *Scientific Reports* **6:** 32969.

Inoue, S. and S. Kondo. 2016. Suture pattern formation in ammonites and the unknown rear mantle structure. *Scientific Reports* **6:** 33686.

Jiang, X., H. Lu, S. Shigeno, L. H. Tan, Y. Yang, C. W. Ragsdale, and J. H. Gao. 2013. Octopus visual system: A functional MRI model for detecting neuronal electric currents without a blood-oxygen-level-dependent confound. *Magnetic Resonance in Medicine* **72:** 1311–1319.

Jochum, A., R. Slapnik, M. Kampschulte, G. Martels, M. Heneka, and B. Páll-Gergely. 2014. A review of the microgastropod genus *Systenostoma* Bavay & Dautzenberg, 1908 and a new subterranean species from China (Gastropoda, Pulmonata, Hypselostomatidae). *ZooKeys* **410:** 23–40.

Jochum, A., L. Prozorova, M. Sharyi-ool, and B. Páll-Gergely. 2015. A new member of troglobitic Carychiidae, *Koreozospeum nodongense* gen. et sp. n. (Gastropoda, Eupulmonata, Ellobioidea) is described from Korea. *ZooKeys* **517:** 39–57.

Jochum, A., A. M. Weigand, E. Bochud, T. Inäbnit, D. D. Dörge, B. Ruthensteiner, A. Favre, G. Martels, and M. Kampschulte.

2017. Three new species of *Carychium* O.F. Müller, 1773 from the Southeastern USA, Belize and Panama are described using computer tomography (CT) (Eupulmonata, Ellobioidea, Carychiidae). *ZooKeys* **675:** 97–127.

Keklikoglou, K., E. Chatzinikolaou, S. Faulwetter, P. Grigoriou, N. Papageorgiou, A. Queirós, S. Rühl, and H. Schmidbaur. 2015. Revealing effects of ocean acidification on the calcified structures of marine invertebrates through micro-computed tomography (micro-CT). *In*: Micro-CT 2015 User Meeting Abstract Book. Pp. 15–25.

Kerbl, A., S. Handschuh, M. T. Nödl, B. Metscher, M. Walzl, and A. Wanninger. 2013. Micro-CT in cephalopod research: Investigating the internal anatomy of a sepiolid squid using a non-destructive technique with special focus on the ganglionic system. *Journal of Experimental Marine Biology and Ecology* **447:** 140–148.

Kocot, K. M., J. T. Cannon, C. Todt, M. R. Citarella, A. B. Kohn, A. Meyer, S. R. Santos, C. Schander, L. L. Moroz, B. Lieb, and K. M. Halanych. 2011. Phylogenomics reveals deep molluscan relationships. *Nature* **477:** 452–456.

Kocot, K. M., T. H. Struck, J. Merkel, D. S. Waits, C. Todt, P. M. Brannock, D. A. Weese, J. T. Cannon, L. L. Moroz, B. Lieb, and K. M. Halanych. 2017. Phylogenomics of Lophotrochozoa with consideration of systematic error. *Systematic Biology* **66:** 256–282.

Krzemnicki, M. S., C. S. Hanser, and V. Revol. 2017. Simultaneous X-radiography, phase-contrast and darkfield imaging to separate natural from cultured pearls. *The Journal of Gemmology* **35:** 628–638.

Lannig, G., A. S. Cherkasov, H.-O. Pörtner, C. Bock, and I. M. Sokolova. 2008. Cadmium-dependent oxygen limitation affects temperature tolerance in eastern oysters (*Crassostrea virginica* Gmelin). *American Journal of Physiology – Regulatory, Integrative and Comparative Physiology* **294:** R1338–R1346.

Lee, C. H., J. J. Flint, B. Hansen, and S. J. Blackband. 2015. Investigation of the subcellular architecture of L7 neurons of *Aplysia californica* using magnetic resonance microscopy (MRM) at 7.8 microns. *Scientific Reports* **5:** 11147.

Lee, H., A. Tikunov, M. K. Stoskopf, and J. M. Macdonald. 2010. Applications of chemical shift imaging to marine sciences. *Marine Drugs* **8:** 2369–2383.

Lemanis, R., D. Korn, S. Zachow, E. Rybacki, and R. Hoffmann. 2016. The evolution and development of cephalopod chambers and their shape. *PLoS ONE* **11:** e0151404.

Lenihan, J., S. Kvist, R. Fernández, G. Giribet, and A. Ziegler. 2014. A dataset comprising four micro-computed tomography scans of freshly fixed and museum earthworm specimens. *GigaScience* **3:** 6.

Li, L., M. J. Connors, M. Kolle, G. T. England, D. I. Speiser, X. Xiao, J. Aizenberg, and C. Ortiz. 2015. Multifunctionality of chiton biomineralized armor with an integrated visual system. *Science* **350:** 952–956.

Li, Z., J. A. Clarke, R. A. Ketcham, M. W. Colbert, and F. Yan. 2015. An investigation of the efficacy and mechanism of contrast-enhanced X-ray computed tomography utilizing iodine for large specimens through experimental and simulation approaches. *BMC Physiology* **15:** 5.

Li, Z., R. A. Ketcham, F. Yan, J. A. Maisano, and J. A. Clarke. 2016. Comparison and evaluation of the effectiveness of two approaches of diffusible iodine-based contrast-enhanced computed tomography (diceCT) for avian cephalic material. *Journal of Experimental Zoology B (Molecular and Developmental Evolution)* **326:** 352–362.

Liew, T. S., A. C. M. Kok, M. Schilthuizen, and S. Urdy. 2014. On growth and form of irregular coiled-shell of a terrestrial snail: *Plectostoma concinnum* (Fulton, 1901) (Mollusca: Caenogastropoda: Diplommatinidae). *PeerJ* **2:** e383.

Liew, T. S. and M. Schilthuizen. 2016. A method for quantifying, visualizing, and analyzing gastropod shell form. *PLoS ONE* **11:** e0157069.

Limaye, A. 2012. Drishti, a volume exploration and presentation tool. *Developments in X-ray Tomography VIII* **8506:** 85060X.

Liu, Y. C., W. S. Chung, C. C. Yu, S. T. Hsu, F. L. Chan, T. S. Liu, C. H. Su, Y. Hwu, N. J. Marshall, and C. C. Chiao. 2018. Morphological changes of the optic lobe from late embryonic to adult stages in oval squids *Sepioteuthis lessoniana*. *Journal of Morphology* **279:** 75–85.

Liu, Y. C., T. H. Liu, C. H. Su, and C. C. Chiao. 2017. Neural organization of the optic lobe changes steadily from late embryonic stage to adulthood in cuttlefish *Sepia pharaonis*. *Frontiers in Physiology* **8:** 538.

Lucocq, J. M., T. M. Mayhew, Y. Schwab, A. M. Steyer, and C. Hacker. 2014. Systems biology in 3D space – enter the morphome. *Trends in Cell Biology* **25:** 59–64.

Lukeneder, A. 2012. Computed 3D visualization of an extinct cephalopod using computer tomographs. *Computers & Geosciences* **45:** 68–74.

Machado, F. M., F. D. Passos, and G. Giribet. 2018. The use of micro-computed tomography as a minimally invasive tool for anatomical study of bivalves (Mollusca: Bivalvia). *Zoological Journal of the Linnean Society*, doi: 10.1093/zoolinnean/zly054.

Marxen, J. C., O. Prymak, F. Beckmann, F. Neues, and M. Epple. 2008. Embryonic shell formation in the snail *Biomphalaria glabrata*: A comparison between scanning electron microscopy (SEM) and synchrotron radiation micro computer tomography (SRμCT). *Journal of Molluscan Studies* **74:** 19–25.

Melzner, F., C. Bock, and H.-O. Pörtner. 2006. Critical temperatures in the cephalopod *Sepia officinalis* investigated using *in vivo* ^{31}P NMR spectroscopy. *The Journal of Experimental Biology* **209:** 891–906.

Melzner, F., C. Bock, and H.-O. Pörtner. 2007. Coordination between ventilator pressure oscillations and venous return in the cephalopod *Sepia officinalis* under control conditions, spontaneous exercise and recovery. *Journal of Comparative Physiology B* **177:** 1–17.

Metscher, B. D. 2009. MicroCT for comparative morphology: Simple staining methods allow high-contrast 3D imaging of diverse non-mineralized animal tissues. *BMC Physiology* **9:** 11.

Mietchen, D., H. Keupp, B. Manz, and F. Volke. 2005. Non-invasive diagnostics in fossils – magnetic resonance imaging of pathological belemnites. *Biogeosciences* **2:** 133–140.

Mietchen, D., M. Aberhan, B. Manz, O. Hampe, B. Mohr, C. Neumann, and F. Volke. 2008. Three-dimensional magnetic resonance imaging of fossils across taxa. *Biogeosciences* **5:** 25–41.

Moles, J., H. Wägele, M. Ballesteros, Á. Pujals, G. Uhl, and C. Avila. 2016. The end of the cold loneliness: 3D comparison between *Doto antarctica* and a new sympatric species of *Doto* (Heterobranchia: Nudibranchia). *PLoS ONE* **11:** e0157941.

Moles, J., H. Wägele, G. Uhl, and C. Avila. 2017. Bipolarity in sea slugs: A new species of *Doridunculus* (Mollusca: Nudibranchia: Onchidoridoidea) from Antarctica. *Organisms Diversity & Evolution* **17:** 101–109.

Mooney, T. A., R. T. Hanlon, J. Christensen-Dalsgaard, P. T. Madsen, D. R. Ketten, and P. E. Nachtigall. 2010. Sound detection by the longfin squid (*Loligo pealeii*) studied with auditory evoked potentials: Sensitivity to low-frequency particle motion and not pressure. *The Journal of Experimental Biology* **213:** 3748–3759.

Neustadter, D. M., R. F. Drushel, and H. J. Chiel. 2002. Kinematics of the buccal mass during swallowing based on magnetic resonance imaging in intact, behaving *Aplysia californica*. *The Journal of Experimental Biology* **205:** 939–958.

Noshita, K. 2014. Quantification and geometric analysis of coiling patterns in gastropod shells based on 3D and 2D image data. *Journal of Theoretical Biology* **363:** 93–104.

Noshita, K., K. Shimizu, and T. Sasaki. 2016. Geometric analysis and estimation of the growth rate gradient on gastropod shells. *Journal of Theoretical Biology* **389:** 11–19.

Novakovic, V. A., G. P. Sutton, D. M. Neustadter, R. D. Beer, and H. J. Chiel. 2006. Mechanical reconfiguration mediates swallowing and rejection in *Aplysia californica*. *Journal of Comparative Physiology A* **192:** 857–870.

Palmer, B. A., G. J. Taylor, V. Brumfeld, D. Gur, M. Shemesh, N. Elad, A. Osherov, D. Oron, S. Weiner, and L. Addadi. 2017. The image-forming mirror in the eye of the scallop. *Science* **358:** 1172–1175.

Paredes, U. M., R. Prys-Jones, M. Adams, J. Groombridge, S. Kundu, P.-M. Agapow, and R. L. Abel. 2012. Micro-CT X-rays do not fragment DNA in preserved bird skins. *Journal of Zoological Systematics and Evolutionary Research* **50:** 247–250.

Pauwels, E., D. van Loo, P. Cornillie, L. Brabant, and L. van Hoorebeke. 2013. An exploratory study of contrast agents for soft tissue visualization by means of high resolution X-ray computed tomography imaging. *Journal of Microscopy* **250:** 21–31.

Pedrouzo, L., Ó. García-Álvarez, V. Urgorri, and M. Pérez-Senaris. 2018. New data and 3D reconstruction of four species of Pruvotinidae (Mollusca: Solenogastres) from the NW Iberian peninsula. *Marine Biodiversity,* doi: 10.1007/s12526-017-0793-1

Pouvreau, S., M. Rambeau, J. C. Cochard, and R. Robert. 2006. Investigation of marine bivalve morphology by in vivo MR imaging: First anatomical results of a promising technique. *Aquaculture* **259:** 415–423.

Quast, M. J., H. Neumeister, E. L. Ezell, and B. U. Budelmann. 2001. MR microscopy of cobalt-labeled nerve cells and pathways in an invertebrate brain (*Sepia officinalis*, Cephalopoda). *Magnetic Resonance in Medicine* **45:** 575–579.

Quintarelli, G., R. Zito, and J. A. Cifonelli. 1971. On phosphotungstic acid staining. I. *The Journal of Histochemistry and Cytochemistry* **19:** 641–647.

Quintarelli, G., M. Bellocci, and R. Geremia. 1973. On phosphotungstic acid staining IV. Selectivity of the staining reaction. *The Journal of Histochemistry and Cytochemistry* **21:** 155–160.

Rosenberg, G. 2014. A new critical estimate of named species-level diversity of the recent Mollusca. *American Malacological Bulletin* **32:** 308–322.

Ruthensteiner, B., N. Baeumler, and D. G. Barnes. 2010. Interactive 3D volume rendering in biomedical publications. *Micron* **41:** 886.e1–886.e17.

Saccomano, M., J. Albers, G. Tromba, M. D. Radmilović, D. Gajović, F. Alves, and C. Dullin. 2018. Synchrotron inline phase contrast μCT enables detailed virtual histology of embedded soft-tissue samples with and without staining. *Journal of Synchrotron Radiation* **25:** 1153–1161.

Schindelin, J., I. Arganda-Carreras, E. Frise, V. Kaynig, M. Longair, T. Pietzsch, S. Preibisch, C. Rueden, S. Saalfeld, B. Schmid, J.-Y. Tinevez, D. J. White, V. Hartenstein, K. Eliceiri, P. Tomancak, and A. Cardona. 2012. Fiji: An open-source platform for biological-image analysis. *Nature Methods* **9:** 676–682.

Schmidbaur, H., K. Keklikoglou, B. D. Metscher, and S. Faulwetter. 2015. Exploring methods to remove iodine and phosphotungstic acid stains from zoological specimens. *In*: Micro-CT 2015 User Meeting Abstract Book. Pp. 109–116.

Seo, E., K. Ohishi, T. Maruyama, Y. Imaizumi-Ohashi, M. Murakami, and Y. Seo. 2014. Testing the constant-volume hypothesis by magnetic resonance imaging of *Mytilus galloprovincialis* heart. *The Journal of Experimental Biology* **217:** 967–973.

Shea, E. K., A. Ziegler, C. Faber, and T. M. Shank. 2018. Dumbo octopod hatchling provides insight into early cirrate life cycle. *Current Biology* **28:** R144–R145.

Sigl, R., H. Imhof, M. Settles, and C. Laforsch. 2013. A novel, non-invasive and in vivo approach to determine morphometric data in starfish. *Journal of Experimental Marine Biology and Ecology* **449:** 1–9.

Sigwart, J. D. and D. R. Lindberg. 2015. Consensus and confusion in molluscan trees: Evaluating morphological and molecular phylogenies. *Systematic Biology* **64:** 384–395.

Smith, P. T. and N. Reddy. 2012. Application of magnetic resonance imaging (MRI) to study the anatomy and reproductive condition of live Sydney rock oyster, *Saccostrea glomerata* (Gould). *Aquaculture* **334-337:** 191–198.

Smith, S. A., N. G. Wilson, F. E. Goetz, C. Feehery, S. C. S. Andrade, G. W. Rouse, G. Giribet, and C. W. Dunn. 2011. Resolving the evolutionary relationships of molluscs with phylogenomic tools. *Nature* **480:** 364–367.

Smith, S. A., N. G. Wilson, F. E. Goetz, C. Feehery, S. C. S. Andrade, G. W. Rouse, G. Giribet, and C. W. Dunn. 2013. Corrigendum: Resolving the evolutionary relationships of molluscs with phylogenomic tools. *Nature* **493:** 708.

Sombke, A., E. Lipke, P. Michalik, G. Uhl, and S. Harzsch. 2015. Potential and limitations of X-ray micro-computed tomography in arthropod neuroanatomy: A methodological and comparative survey. *The Journal of Comparative Neurology* **523:** 1281–1295.

Sukhotin, A., N. Fokina, T. Ruokolainen, C. Bock, H.-O. Pörtner, and G. Lannig. 2017. Does the membrane pacemaker theory of metabolism explain the size dependence of metabolic rate in marine mussels? *The Journal of Experimental Biology* **220:** 1423–1434.

Sumner-Rooney, L. and J. D. Sigwart. 2017. Lazarus in the museum: Resurrecting historic specimens through new technology. *Invertebrate Zoology* **14:** 73–84.

Sutton, M. D. 2008. Tomographic techniques for the study of exceptionally preserved fossils. *Proceedings of the Royal Society B* **275:** 1587–1593.

Sutton, M. D. and J. D. Sigwart. 2012. A chiton without a foot. *Palaeontology* **55:** 401–411.

Tramacere, F., L. Beccai, M. Kuba, A. Gozzi, A. Bifone, and B. Mazzolai. 2013. The morphology and adhesion mechanism of *Octopus vulgaris* suckers. *PLoS ONE* **8:** e65074.

Ukmar-Godec, T., G. Kapun, P. Zaslansky, and D. Fauvre. 2015. The giant keyhole limpet radular teeth: A naturally-grown harvest machine. *Journal of Structural Biology* **192:** 392–402.

Vendrasco, M. J., T. E. Wood, and B. N. Runnegar. 2004. Articulated palaeozoic fossil with 17 plates greatly expands disparity of early chitons. *Nature* **429:** 288–291.

Vickerton, P., J. Jarvis, and N. Jeffery. 2013. Concentration-dependent specimen shrinkage in iodine-enhanced microCT. *Journal of Anatomy* **223:** 185–193.

Vinther, J. 2015. The origins of molluscs. *Palaeontology* **58:** 19–34.

von Brand, E., M. Cisterna, G. Merino, E. Uribe, C. Palma-Rojas, M. Rosenblitt, and J. L. Albornoz. 2009. Non-destructive method to study the internal anatomy of the Chilean scallop *Argopecten purpuratus*. *Journal of Shellfish Research* **28:** 325–327.

Wanek, J. and F. J. Rühli. 2016. Risk to fragmented DNA in dry, wet, and frozen states from computed tomography: A comparative theoretical study. *Radiation and Environmental Biophysics* **55:** 229–241.

Wanninger, A. 2015. Morphology is dead – long live morphology! Integrating morphoevodevo into molecular evodevo and phylogenomics. *Frontiers in Ecology and Evolution* **3:** 54.

Wanninger, A. and T. Wollesen. 2018. The evolution of molluscs. *Biological Reviews*, doi: 10.1111/brv.12439

Werner, R., K. Hoernle, F. Hauff, M. Portnyagin, G. Yogodzinski, and A. Ziegler. 2016. RV SONNE Fahrtbericht / cruise report SO 249 BERING – origin and evolution of the Bering Sea: An integrated geochronological, volcanological, petrological and geochemical approach. *GEOMAR Report N. Ser.* **30:** 1–89.

Xavier, J. C., A. L. Allcock, Y. Cherel, M. R. Lipinski, G. J. Pierce, P. G. K. Rodhouse, R. Rosa, E. K. Shea, J. M. Strugnell, E. A. G. Vidal, R. Villanueva, and A. Ziegler. 2015. Future challenges in cephalopod research. *Journal of the Marine Biological Association of the United Kingdom* **95:** 999–1015.

Yang, W., L. Duan, G. Chen, L. Xiong, and Q. Liu. 2013. Plant phenomics and high-throughput phenotyping: Accelerating rice functional genomics using multidisciplinary technologies. *Current Opinion in Plant Biology* **16:** 180–187.

Zanette, I., G. Daghfous, T. Weitkamp, B. Gillet, D. Adriaens, M. Langer, P. Cloetens, L. Helfen, A. Bravin, F. Peyrin, T. Baukbach, J. M. Dischler, D. Van Loo, T. Praet, M. Poirier-Quinot, and R. Boistel. 2014. Looking inside marine organisms with magnetic resonance and X-ray imaging. *In*: E. G. Reynaud, ed., *Imaging Marine Life: Macrophotography and Microscopy Approaches for Marine Biology*. Wiley-VCH, Weinheim. Pp. 123–184.

Zehbe, R., A. Haibel, H. Riesenmeier, U. Gross, C. J. Kirkpatrick, H. Schubert, and C. Brochhausen. 2010. Going beyond histology. Synchrotron micro-computed tomography as a methodology for biological tissue characterization: From tissue morphology to individual cells. *Journal of the Royal Society Interface* **7:** 49–59.

Ziegler, A. 2012. Broad application of non-invasive imaging techniques to echinoids and other echinoderm taxa. *Zoosymposia* **7:** 53–70.

Ziegler, A., C. Bock, D. R. Ketten, R. W. Mair, S. Mueller, N. Nagelmann, E. D. Pracht, and L. Schröder. 2018. Digital three-dimensional imaging techniques provide new analytical pathways for malacological research. Morphobank project #3107, doi: 10.7934/P3107

Ziegler, A., C. Faber, S. Mueller, and T. Bartolomaeus. 2008. Systematic comparison and reconstruction of sea urchin (Echinoidea) internal anatomy: A novel approach using magnetic resonance imaging. *BMC Biology* **6:** 33.

Ziegler, A., C. Faber, S. Mueller, N. Nagelmann, and L. Schröder. 2014. A dataset comprising 141 magnetic resonance imaging scans of 98 extant sea urchin species. *GigaScience* **3:** 21.

Ziegler, A., M. Kunth, S. Mueller, C. Bock, R. Pohmann, L. Schröder, C. Faber, and G. Giribet. 2011. Application of magnetic resonance imaging in zoology. *Zoomorphology* **130:** 227–254.

Ziegler, A. and B. H. Menze. 2013. Accelerated acquisition, visualization, and analysis of zoo-anatomical data. *In*: J. Zander and P. J. Mosterman, eds., *Computation for Humanity: Information Technology to Advance Society*. CRC Press, Boca Raton. Pp. 233–261.

Ziegler, A. and S. Mueller. 2011. Analysis of freshly fixed and museum invertebrate specimens using high-resolution, high-throughput MRI. *Methods in Molecular Biology* **771:** 633–651.

Ziegler, A., M. Ogurreck, T. Steinke, F. Beckmann, S. Prohaska, and A. Ziegler. 2010. Opportunities and challenges for digital morphology. *Biology Direct* **5:** 45.

Submitted: 1 May 2018; **accepted:** 10 November 2018; **final revisions received:** 12 November 2018